HAL open science

BhaBAR: Big Halpha kinematical sample of BARred spiral galaxies - I. Fabry-Perot Observations of 21 galaxies

O. Hernandez, C. Carignan, P. Amram, L. Chemin, O. Daigle

▶ **To cite this version:**

O. Hernandez, C. Carignan, P. Amram, L. Chemin, O. Daigle. BhaBAR: Big Halpha kinematical sample of BARred spiral galaxies - I. Fabry-Perot Observations of 21 galaxies. Monthly Notices of the Royal Astronomical Society, 2005, 360 Issue 4, pp.1201. 10.1111/j.1365-2966.2005.09125.x . hal-00014446

HAL Id: hal-00014446

https://hal.science/hal-00014446v1

Submitted on 26 Jan 2021

HAL is a multi-disciplinary open access archive for the deposit and dissemination of scientific research documents, whether they are published or not. The documents may come from teaching and research institutions in France or abroad, or from public or private research centers.

L'archive ouverte pluridisciplinaire **HAL**, est destinée au dépôt et à la diffusion de documents scientifiques de niveau recherche, publiés ou non, émanant des établissements d'enseignement et de recherche français ou étrangers, des laboratoires publics ou privés.

Mon. Not. R. Astron. Soc. **360,** 1201–1230 (2005) doi:10.1111/j.1365-2966.2005.09125.x

BHαBAR: big Hα kinematical sample of barred spiral galaxies – I. Fabry–Perot observations of 21 galaxies

O. Hernandez,[1,2★]† C. Carignan,[1★] P. Amram,[2★] L. Chemin[1] and O. Daigle[1★]

[1]*Observatoire du mont Mégantic, LAE, Université de Montréal, CP 6128 succ. centre ville, Montréal, Québec, Canada H3C 3J7*
[2]*Observatoire Astronomique de Marseille Provence et LAM, 2 pl. Le Verrier, 13248 Marseille Cedex 04, France*

Accepted 2005 April 14. Received 2005 April 6; in original form 2005 January 13

ABSTRACT

We present the Hα gas kinematics of 21 representative barred spiral galaxies belonging to the BHαBAR sample. The galaxies were observed with FaNTOmM, a Fabry–Perot integral-field spectrometer, on three different telescopes. The three-dimensional data cubes were processed through a robust pipeline with the aim of providing the most homogeneous and accurate data set possible useful for further analysis. The data cubes were spatially binned to a constant signal-to-noise ratio, typically around 7. Maps of the monochromatic Hα emission line and of the velocity field were generated and the kinematical parameters were derived for the whole sample using tilted-ring models. The photometrical and kinematical parameters (position angle of the major axis, inclination, systemic velocity and kinematical centre) are in relative good agreement, except perhaps for the later-type spirals.

Key words: methods: observational – techniques: radial velocities – galaxies: fundamental parameters – galaxies: kinematics and dynamics – galaxies: spiral.

1 INTRODUCTION

The presence of a bar in disc galaxies seems to be a common feature. Bars have been recognized in galaxies since the time of Curtis (1918) and Hubble (1926). In the optical, roughly 30 per cent of spiral galaxies are strongly barred (de Vaucouleurs 1963) while another 25 per cent are weakly barred. Evidence that bars in spirals are more obvious in the near-infrared (NIR) than in the visible goes back to Hackwell & Schweizer (1983). Recent surveys in the NIR have shown that up to 75 per cent of high surface brightness galaxies may have a more or less strong bar (e.g. Eskridge et al. 2000; Knapen, Shlosman & Peletier 2000b).

When present, such bars will introduce non-circular motions that should be seen in the radial velocity fields. Because the kinematics of barred spirals is different from that of more or less axisymmetric discs, it is important to model them properly if we want to derive, as accurately as possible, the overall mass distribution. This distribution is directly derived from the knowledge of the circular velocities. Because the gas in axisymmetric galaxies is nearly on circular orbits, and its random motions are small compared with the rotation, its kinematics can be used to derive rotation curves (RCs). However, when a galaxy is barred, the gas response to the non-axisymmetric part of the potential cannot be neglected. Thus, an RC derived without correcting for those non-circular motions cannot be said to represent the circular motions and be used to derive the mass distribution.

The presence of a bar is expected to leave signatures mainly in the central regions of the RCs (Bosma 1981b; Athanassoula 1984; Combes & Gerin 1985; Schoenmakers, Franx & de Zeeuw 1997; Athanassoula & Misiriotis 2002), which is the region where the free parameters of the mass models are really constrained (Blais-Ouellette et al. 1999, 2004; Blais-Ouellette, Amram & Carignan 2001). Indeed, the parameters of mass models are not constrained by the flat part but by the rising part of RCs.

Bars in galaxies have very different masses, lengths, axial ratios, colour distributions, gas content, pattern speeds, shapes and kinematics. The determination of the fundamental bar parameters is a delicate task. Even if the observational constraints are numerous, their determinations are rarely unambiguous. Difficulties come from the following.

(i) The various galactic components (bar, disc, spiral arms, bulge, rings) are closely imbricated in disc galaxies: observations as well as models integrate the various components and it is not possible to observe them separately.

(ii) Three-dimensional (3D) shapes in galaxies are observed projected on the plane of the sky and their deprojection is not unambiguous, particularly for barred galaxies.

(iii) The parameters of bars depend on the luminous to dark matter ratio distribution, e.g. galaxies having initially the same disc and the same halo-to-disc mass ratio but different central halo concentrations have very different properties (Athanassoula & Misiriotis 2002).

★Visiting Astronomer, Canada–France–Hawaii Telescope, operated by the National Research Council of Canada, the Centre National de la Recherche Scientifique de France, and the University of Hawaii.
†E-mail: olivier@astro.umontreal.ca

© 2005 RAS

Downloaded from https://academic.oup.com/mnras/article/360/4/1201/1076455 by CNRS - ISTO user on 26 January 2021

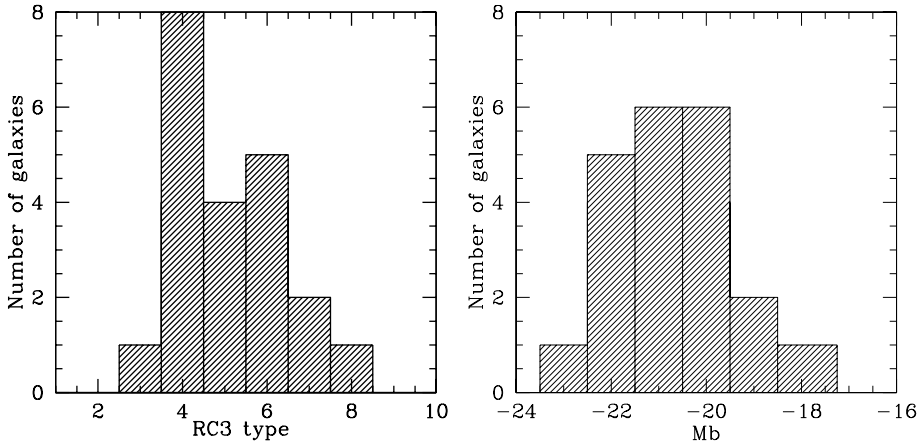

Figure 1. Histogram of the sample morphological types and M_B. Left: the type goes from SBb (type 3) to SBdm (type 8). Right: M_B varies from −17 to −23.

Bars observed from two-dimensional (2D) radial velocity fields contain a fraction of hidden information in tracing the total mass distribution (luminous and dark) and they may be directly compared to N-body + smoothed particle hydrodynamics (SPH) simulations. Moreover, the signature of the bar can appear more significantly through the 2D gaseous velocity field (non-symmetrical features due to gas chocs, star formation regions of high density) than through the stellar one. So, 2D gaseous velocity fields give a valuable additional observational information that will help to disentangle the parameters of the bar.

For instance, the existence of a velocity gradient along the minor axis, in both the stellar and the gaseous 2D velocity fields, is not a very good criterion to pick out bars, while the angles between the kinematical major and minor axes and the twists of the isovelocity contours are better criteria (Bosma 1981b).

Table 1. Observational data for the BHαBAR sample. D denotes distances in Mpc. $D_{25}^{b,i}$ is the optical diameter at 25 mag arcsec^{-2} in B. $M_B^{b,i}$ is the absolute magnitude in B. $B_T^{b,i}$ is the apparent magnitude in B. $L_b^{b,i}$ is bar lengths from Martin (1995), all adjusted for the effects of projection and obscuration. PA_b is the position angle of the bar. V_{sys} are systemic velocities provided by Tully (1988). The symbol * refers to a nuclear activity. Kpn04 refers to Knapen et al. (2004), and Kpn03 refers to Knapen et al. (2003).

Galaxy name	α(J2000) (h m s)	δ(J2000) (° ′ ″)	Type RC3	D (Mpc)	$D_{25}^{b,i}$ (arcmin)	$M_B^{b,i}$	$B_T^{b,i}$	$L_b^{b,i}$ (arcsec)	$\mathrm{PA_b}$ (°)	V_{sys}	Image sources B	NIR
NGC 0925	02 27 16.8	+33 34 41	SAB(s)d	9.3[a]	11.2	−20.0	10.6	56.5	112	554	XDSS	Spitzer
IC 0342	03 46 49.7	+68 05 45	SAB(rs)cd	3.9[b]	27.9	−21.6	6.4	n/a[c]	32	32	XDSS	2MASS
NGC 1530	04 23 28.5	+75 17 50	SB(rs)b	36.6[b]	4.8	−21.3	11.5	137.0[c]	116	2460	XDSS	2MASS
NGC 2336	07 27 04.5	+80 10 41	SAB(r)bc	22.9[b]	5.2	−22.1	11.1	72.8	5	2196	XDSS	2MASS
NGC 2403	07 36 54.5	+65 35 58	SAB(s)cd	4.2[a]	21.4	−19.7	8.5	n/a[c]	n/a	132	XDSS	Spitzer
NCG 2903	09 32 09.7	+21 30 02	SB(s)bc	6.3[b]	10.0	−19.8	9.13	143.4	26	554	XDSS	2MASS
NGC 3198	10 19 54.9	+45 33 09	SB(rs)c	14.5[a]	7.8	−20.2	11.1	81.8	12	660	XDSS	Spitzer
NCG 3359	10 46 37.7	+63 13 22	SB(rs)c	19.2[b]	7.2	−20.4	10.8	87.0	15	1013	XDSS	2MASS
NGC 3953	11 53 49.5	+52 19 39	SB(r)bc	17.0[b]	5.2	−20.6	10.5	70.6	55	1054	XDSS	2MASS
NGC 3992	11 57 36.0	+53 22 28	SB(rs)bc	17.0[b]	6.6	−20.7	10.4	136.5	37	1051	XDSS	2MASS
NGC 4236	12 16 42.1	+69 27 45	SB(s)dm	2.2[b]	16.4	−17.3	9.5	170.7	143	2	XDSS	2MASS
NGC 4321	12 22 55.2	+15 49 23	SAB(s)bc	16.1[a]	7.4	−22.1	10.0	53.4	107	1590	Kpn04	Spitzer
NGC 4535	12 34 20.3	+08 11 53	SAB(s)c	16.0[a]	6.9	−22.0	10.6	70.0[c]	45	1966	Kpn04	Kpn03
NGC 5371	13 55 40.6	+40 27 44	SAB(rs)bc	37.8[b]	4.0	−21.6	11.3	47.2	97	2558	XDSS	2MASS
NGC 5457	14 03 12.5	+54 20 55	SAB(rs)cd	7.4[a]	30.2	−22.7	8.3	86.5	84	231	XDSS	2MASS
NGC 5921	15 21 56.4	+05 04 11	SB(r)bc	25.2[b]	4.9	−20.7	11.3	73.5	21	1480	XDSS	2MASS
NGC 5964	15 37 36.3	+05 58 28	SB(rs)d	24.7[b]	4.0	−19.5	12.5	56.0[c]	150	1447	Kpn04	Kpn03
NGC 6217	16 32 39.2	+78 11 53	(R)SB(rs)bc*	23.9[b]	3.6	−20.2	11.7	68.8	153	1359	XDSS	2MASS
NGC 6946	20 34 52.0	+60 09 15	SAB(rs)cd	5.5[b]	14.9	−20.8	7.92	34.5	166	46	Kpn04	Spitzer
NGC 7479	23 04 57.1	+12 19 18	SB(s)c*	32.4[b]	3.8	−21.1	11.4	114.7	2	2382	XDSS	2MASS
NGC 7741	23 43 54.0	+26 04 32	SB(s)cd	12.3[b]	3.8	−18.8	11.7	89.0	103	750	Kpn04	Kpn03

[a]Distances calculated from Cepheids: NGC 0925 (Silbermann et al. 1994); NGC 2403 (Freedman & Madore 1988); NGC 3198 (Kelson et al. 1999); NGC 4321 (Ferrarese et al. 1996); NGC 4535 (Macri et al. 1999); NGC 5457 (Kelson et al. 1996).

[b]Distances are based on velocities, an assumed value of the Hubble constant of 75 km s^{-1} Mpc^{-1}, and the model that describes the velocity perturbations in the vicinity of the Virgo Cluster (cf. Tully 1988).

[c]Values not available in Martin (1995) are calculated from isophote fitting (except for NGC 1530 where the data are from Zurita et al. 2004).

Downloaded from https://academic.oup.com/mnras/article/360/4/1201/1076455 by CNRS - ISTO user on 26 January 2021

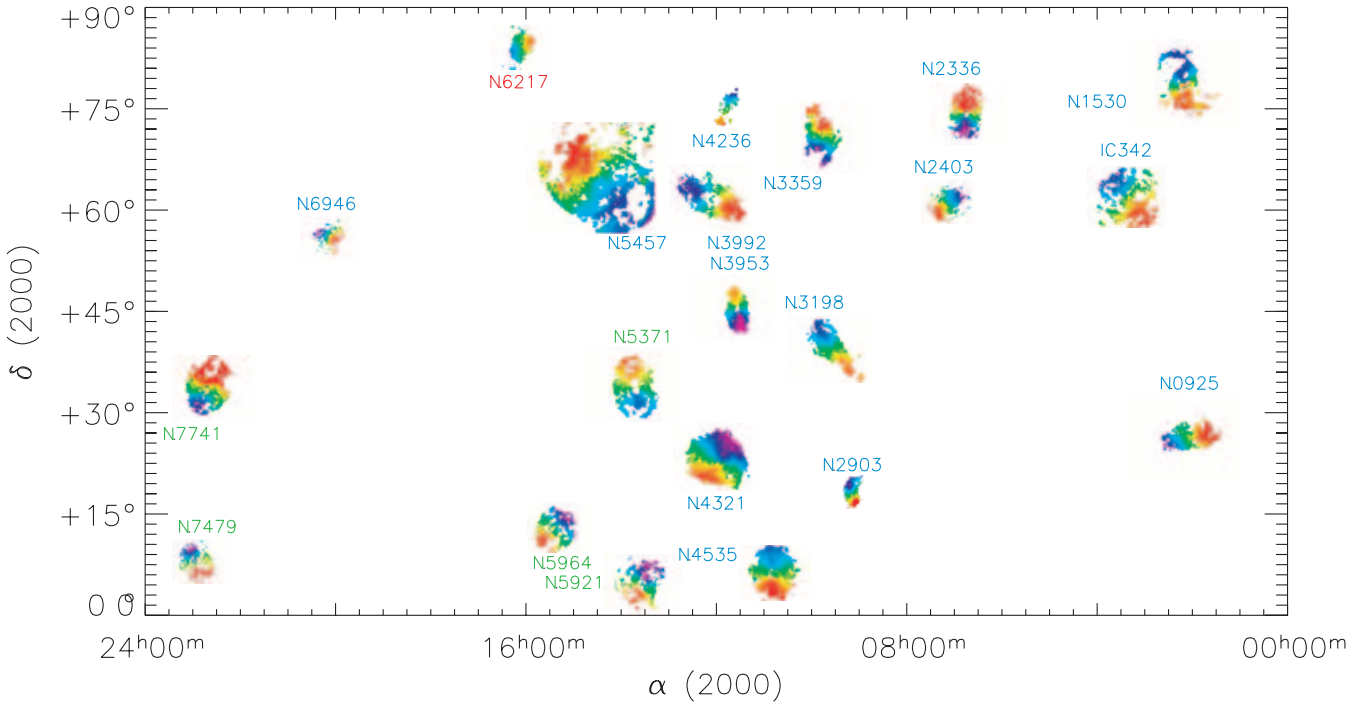

Figure 2. The BHαBAR sample sky coverage. The names in blue correspond to the observations carried out at the OmM, in green at the CFHT and in red at the OHP. The respective sizes of the galaxies given in kpc can be directly compared.

Theoretical predictions from *N*-body simulations (e.g. Kormendy 1983; Lütticke, Dettmar & Pohlen 2000; Athanassoula & Misiriotis 2002) may be summarized as follows.

(i) When the position angle of the bar is roughly parallel to the major axis, the isovelocities show a characteristic concentration towards the central region due to the fact that particle orbits are elongated along the bar and the velocity along an orbit is larger at pericentre than at apocentre.

(ii) When the position angle of the bar is intermediate between the major and minor axis position angles, the velocity field shows the 'Z' structure characteristic of barred galaxy velocity fields (see, for example, Peterson et al. 1978, for NGC 5383).

(iii) When the position angle of the bar is roughly parallel to the minor axis, the velocity field shows a sizeable area of solid body rotation in the inner parts.

In the case of a dark halo more concentrated in the central regions of the galaxy, several of these features remain but some notable differences appear (Athanassoula & Misiriotis 2002).

Table 2. FaNTOmM characteristics on various telescopes. F/D represents the ratio focal length over telescope diameter. The pixel size after binning is 2×2, the original GaAs system providing 1024×1024 pixel^2. FOV is the diagonal field of view of the detector. FOV (vign.) represents the effective unvignetted FOV (without the vignetting due to the filter used).

Telescope name	Focal reducer	F/D	Pixel size (arcsec)	FOV (arcmin)	FOV (vign.) (arcmin)
OmM	PANORAMIX	2.3	1.61	19.4	19.4
OHP	CIGALE	3.92	0.68	8.2	5.5
CFHT	MOS	2.96	0.48	5.8	3.9

(i) When the position angle of the bar is roughly parallel to the major axis, the isovelocities show a strong pinching in the innermost region, on or near the bar minor axis.

(ii) When the position angle of the bar is intermediate between the major and minor axis position angles, the 'Z' shape of the velocity field is much more pronounced.

(iii) When the position angle of the bar is roughly parallel to the minor axis, the innermost solid-body rotation part does not show strong differences; however, as we move away from the kinematical minor axis the isovelocities show a clear wavy pattern, indicating that the mean velocity is lower at the ends of the bar than right above or right below it.

This study is dedicated to the kinematics and the dynamics of barred galaxies. The aim will be to derive the most accurate velocity fields possible for a representative sample of barred galaxies in order to analyse their kinematics. The BHαBAR sample should provide the most homogeneous data set on barred spiral galaxies to date. Once this data base is available, the following goal will be to model these galaxies, extract the non-circular component of the velocities, and thus recover the circular motions and derive proper RCs. Only then will it be possible to model accurately their mass distributions.

In this paper, we present a homogeneous study of the kinematics of 21 nearby barred spiral galaxies, based on the 2D kinematics of the Hα gas. In Section 2 we give an overview of the observational campaign and present the global properties of the BHαBAR sample, while Section 3 we discuss the data reduction and especially the adaptive binning that was performed. In Section 4, the kinematical parameters are derived and the Fabry–Perot (FP) maps are presented in Section 5. The conclusions can be found in Section 6 and an appendix presents a short observational description of the galaxies of the BHαBAR sample.

Downloaded from https://academic.oup.com/mnras/article/360/4/1201/1076455 by CNRS - ISTO user on 26 January 2021

Table 3. Journal of the FP observations. (4) λ_c is the filter central wavelength in Å. (5) $\Delta\lambda$ is the filter full width at half-maximum in Å. (6) T is the filter maximum transmission at λ_c. (7) $t_{\rm tot}$ is the total exposure time in minutes. (8) $t_{\rm ch}$ is the exposure time per channel in minutes. (9) p is the FP interference order at Hα. (10) FSR is the FP free spectral range at Hα in km s^{-1}. (11) F is mean Finesse through the FOV. (12) R is the resolution for a S/N ratio of 5 at the sample step. (13) nch is the number of channels done by cycle in multiplex observations. (14) stp is the wavelength step in Å.

Galaxy	Date	Filter			Exposure		FP				Sampling	
Name		$\lambda_c^{(4)}$	$\Delta\lambda^{(5)}$	T$^{(6)}$	$t_{tot}^{(7)}$	$t_{ch}^{(8)}$	p$^{(9)}$	FSR$^{(10)}$	$F^{(11)}$	$R^{(12)}$	nch$^{(13)}$	stp$^{(14)}$
NCG 0925[a]	02/11/02	6584	15	75	132	2.75	765	391.77	16	12 240	48	0.18
IC 0342[a]	02/11/03	6578	15	60	144	3	765	391.77	16	12 240	48	0.18
NGC 1530[a]	03/01/30	6622	15	70	240	5	899	333.36	20	17 980	48	0.15
NGC 2336[a]	02/11/10	6617	15	69	240	5	765	391.77	16	12 240	48	0.18
NGC 2403[a]	02/11/17	6569	10	50	120	3	765	391.77	14	10 670	40	0.21
NCG 2903[a]	03/02/08	6599	15	74	180	3.75	899	333.36	20	17 980	48	0.15
NGC 3198[a]	03/03/06	6584	15	75	260	5	899	333.36	23	20 976	52	0.14
NCG 3359[a]	01/11/17	6569	10	50	130	3.25	765	391.77	14	10 670	40	0.21
NGC 3953[a]	03/02/26	6599	15	74	273	5.25	899	333.36	23	20 976	52	0.14
NGC 3992[a]	03/02/27	6599	15	74	260	5	899	333.36	23	20 976	52	0.14
NGC 4236[a]	04/02/27	6578	15	60	182	3.5	899	333.36	23	20 976	52	0.14
NGC 4321[a]	03/02/25	6605	15	75	260	5	899	333.36	23	20 976	52	0.14
NGC 4535[a]	03/03/06	6617	15	69	156	3	899	333.36	23	20 976	52	0.14
NGC 5371[b]	03/04/04	6622	15	70	88	1.83	899	333.36	16	17 980	48	0.15
NGC 5457[a]	03/02/28	6578	15	60	260	3.5	899	333.36	23	20 976	52	0.14
NGC 5921[b]	03/04/09	6599	15	74	120	2.5	899	333.36	16	17 980	48	0.15
NGC 5964[b]	03/04/08	6599	15	74	120	2.5	899	333.36	16	17 980	48	0.15
NGC 6217[c]	01/10/17	6595	10	60	72	3	793	377.94	11	8722	24	0.34
NGC 6946[a]	02/11/19	6569	10	50	120	2	765	391.77	14	10 670	40	0.21
NGC 7479[b]	02/10/04	6617	15	69	60	6	1162	257.92	11	12 782	24	0.23
NGC 7741[b]	02/10/06	6584	15	75	60	6	1162	257.92	11	12 782	24	0.23

[a]OmM: Observatoire du mont Mégantic, Québec, Canada. 1.6-m telescope. [b]CFHT: Canada–France–Hawaii Telescope, Hawaii, USA. 3.6-m telescope. [c]OHP: Observatoire de Haute-Provence, France. 1.93-m telescope.

2 BHαBAR SAMPLE: OBSERVATIONS

2.1 The sample

The 21 galaxies of the BHαBAR sample were selected among northern ($\delta_{\rm J2000} \geqslant +5.0$) nearby barred galaxies in de Vaucouleurs et al. (1991, hereafter RC3) with systemic velocities $\leqslant$3000 km s^{-1}. Their optical sizes D_{25} were selected to take advantage of the specific field of view (FOV) of the three telescopes used: Observatoire du mont Mégantic (OmM) telescope, $D_{25} \geqslant 3.5$ arcmin; Canada–France–Hawaii Telescope (CFHT), $2.0 \leqslant D_{25} \leqslant 4.3$ arcmin; Observatoire de Haute-Provence (OHP) telescope, $2.0 \leqslant D_{25} \leqslant 6.0$ arcmin.

To avoid problems related to disc opacity around Hα wavelengths, galaxies with inclination >75° have been discarded. The photometrical inclinations i were calculated using $q = b/a$, the ratio of the minor axis to the major axis, extracted from the value of R_{25} given in RC3 and applying the following formula

$$\cos^2 i = \frac{q^2 - q_0^2}{1 - q_0^2},$$

(Bottinelli et al. 1983) where q_0 is the intrinsic axial ratio of the disc (for an edge-on system). q_o was not considered as a function of morphological types because the variation from its nominal value of $q_0 = 0.2$ is only significant for late-type galaxies (types $\geqslant$ Sd) which represent only three of the 21 galaxies in the sample. The selected galaxies reasonably sample the different morphological Hubble types, from SBb (or SABb) to SBdm (or SABdm) and have absolute magnitudes $M_B \leqslant -17$. The idea was to try to obtain a complete and homogeneous coverage of the Hubble sequence. However, due to their poor gas content, only one early-type galaxy (SBb) was observed. At the other end of the sequence, only one Sdm was observed. Fig. 1 gives a histogram of the sample.

The galaxies have also been chosen not to be in obvious interaction with close companions. To construct mass model and to build the gravitational potential in future N-body models, galaxies with available H I data and surface photometry from the literature have been chosen: the photometry comes from Spitzer 3.6-μm and/or J-, H-, $K_{\rm s}$-band high-resolution images (2MASS) or better ground images when available (e.g. Knapen et al. 2003, 2004). Except for two cases which are Seyfert galaxies (NGC 6217 and 7479), the galaxies have no nuclear activity. This confirmation of nuclear activity was not clear at the moment of the selection of the BHαBAR sample, so it was decided to keep them in the sample. This will be taken into account when, in further work, N-body coupled to SPH simulations will be carried out (forthcoming papers).

The global distribution versus morphological type and blue absolute magnitude (M_B) are shown in Fig. 1 and the basic information on the objects can be found in Table 1. The 21 velocity fields of the galaxies are mapped in Fig. 2.

2.2 Observing runs

The observations were obtained using FaNTOmM,[1] which is a permanent instrument on the OmM telescope, and a visitor instrument on various other telescopes. FaNTOmM is a wide integral field

[1] FaNTOmM stands for Fabry–Perot of New Technology of the Observatoire du mont Mégantic (http://www.astro.umontreal.ca/fantomm).

Downloaded from https://academic.oup.com/mnras/article/360/4/1201/1076455 by CNRS - ISTO user on 26 January 2021

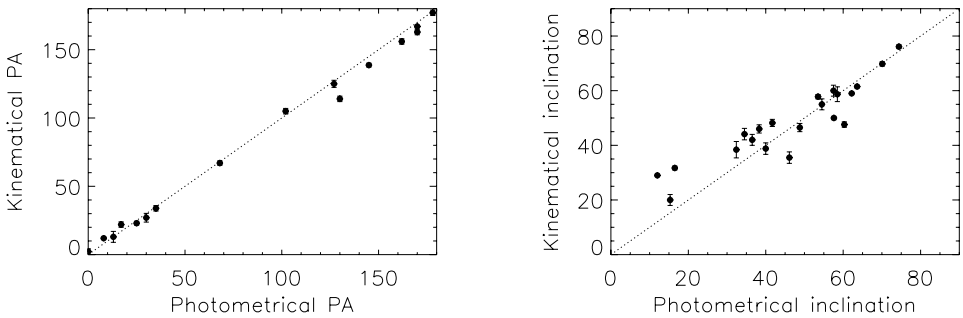

Figure 3. Comparison between the kinematical and photometrical position angles and inclinations. Position angles are given modulo 180°. The dashed line represents the $y = x$ equation.

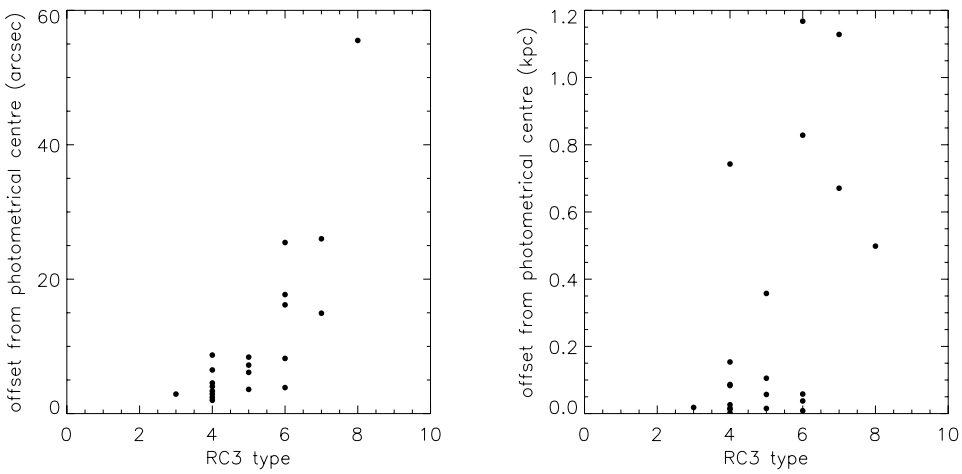

Figure 4. Left: distance (in arcsec) between the photometrical and kinematical centres as a function of morphological type. The offsets are computed in the plane of the sky (not corrected for inclination). Right: deprojected distance (in kpc) between the photometrical and kinematical centres as a function of the morphological type. The offsets have been computed in the plane of the galaxy, using the position angles and the inclinations given in Table 5.

spectrometer made of an image photon counting system (IPCS), a scanning FP and an interference filter. The photocathode used has a high quantum efficiency (∼30 per cent at Hα). FaNTOmM is coupled to the focal reducers of the telescopes used (see details in Table 2).

The IPCS has a third-generation photocathode with high quantum efficiency over a large wavelength range (Gach et al. 2002; Hernandez et al. 2003). This camera is very efficient at reaching good signal-to-noise (S/N) ratio for objects with very faint fluxes because, compared with CCDs, it has no read-out noise. Its multiplex mode also allows a rapid and efficient suppression of the OH sky lines because their variations can be averaged out. FaNTOmM was used in its low spatial resolution mode of 512 × 512 pixel^2 (instead of 1024 pixel^2).

The observations of the sample were spread over nine different observing runs over a 3-yr period. Six runs were at the OmM 1.6-m, one at the OHP 1.93-m and two at the CFHT 3.6-m. Various FP interferometers were used in order to fit the adequate spectral resolution. The interference orders vary from $p = 765$ to $p = 1162$, calculated for $\lambda_0 = 6562.78$ Å (see Table 3).

All the calibrations were performed using the same neon lamp (see below for more details on the data reduction). With the rapid analogic detector mode, calibrations were made in less than a minute. This allowed us to perform as many calibrations as needed during the runs with very little overhead. A new bank of interference filters was also used, covering a velocity range from 0 to 10 000 km s^{-1} (from 6562 to 6785 Å, with $\Delta\lambda \sim 15$ Å).

3 DATA REDUCTION

The reduction of the data cubes was performed using the package ADHOCW (see http://www.oamp.fr/adhoc/adhoc.html; Amram et al. 1992) rewritten with large improvements under the IDL package (Daigle et al. 2005). The major improvements are the following:

(i) the elementary interferograms (elementary images obtained with an exposure time ranging from 10 to 15 s, depending on the sky transparency conditions and on the number of scanning steps) were corrected from sky fluctuations before summation;

(ii) adaptive Hanning smoothing was performed in order to increase the S/N over the field;

(iii) World Coordinate System (WCS) astrometry on the images was performed;

(iv) strong and robust OH night sky line removal was used;

(v) full automated and reproductible reduction and data analysis were performed.

3.1 Phase calibration

Raw interferograms must be corrected to obtain data cubes sorted in wavelengths. This operation is called the 'phase calibration' or

Downloaded from https://academic.oup.com/mnras/article/360/4/1201/1076455 by CNRS - ISTO user on 26 January 2021

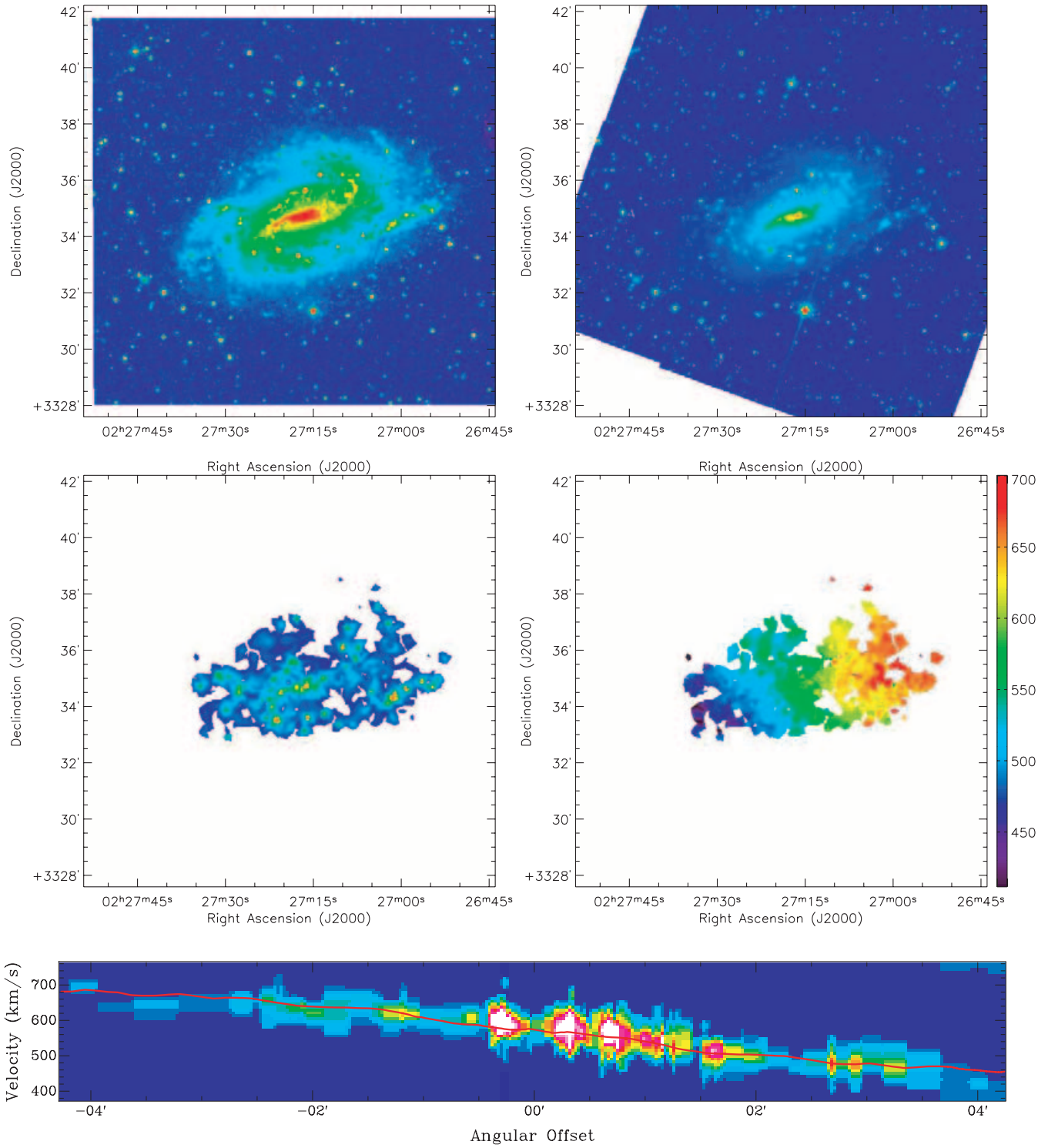

Figure 5. NGC 0925. Top left: XDSS blue-band image. Top right: 3.6-μm Spitzer image. Middle left: Hα monochromatic image. Middle right: Hα velocity field. Bottom: PV diagram. The Hα velocity field and Hα monochromatic image were spatially binned using an adaptive binning. The scale of the colour used to represent the velocity is located to the right of the Hα map. The PV diagram was obtained by integrating over a slit of three pixels wide using the velocities of the model extracted from GIPSY and the data cube from the observations.

wavelength calibration. Those calibrations are obtained by scanning the narrow Ne 6599-Å line under the same conditions as the observations. Two phase calibrations are carried out, one before and the other after the exposure. Using the mean of the calibrations, a 'phase map' is computed. This indicates the scanning step at which is observed the maximum of the interference pattern inside a given pixel. The FP formula below, giving the shape of the interference pattern on the detector as a function of the observed wavelength,

Downloaded from https://academic.oup.com/mnras/article/360/4/1201/1076455 by CNRS - ISTO user on 26 January 2021

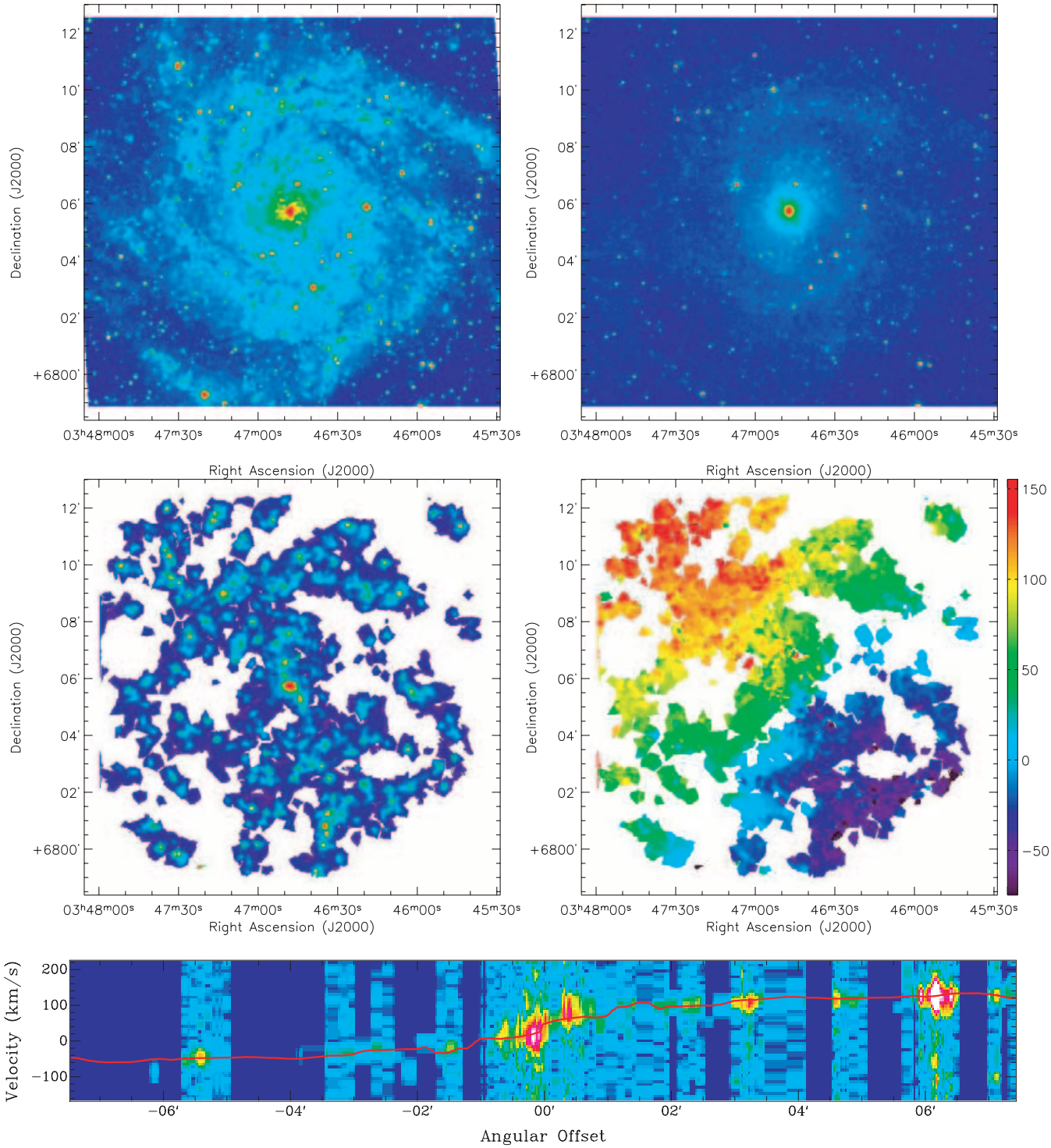

Figure 6. IC 0342. Top left: XDSS blue-band image. Top right: 2MASS K_s-band image. Middle left: Hα monochromatic image. Middle right: Hα velocity field. Bottom: PV diagram.

allows us to find the observed Doppler-shifted wavelength λ at each point by comparison with

$$p\lambda = 2ne\cos\theta.$$

Here, p is the interference order at λ_0 (here 6562.78 Å), n is the index of the medium, e is the distance between the two plates of the FP and θ is the incidence angle on the FP (angular distance on the sky). An uncertainty remains because the velocity is only known modulo the free spectral range (column 10 in Table 3). This ambiguity is easily solved by using comparisons with long-slit spectroscopy or 21-cm H I line data to provide the zero-point of the velocity scale. However, this means that when the redshift emission line of the

Downloaded from https://academic.oup.com/mnras/article/360/4/1201/1076455 by CNRS - ISTO user on 26 January 2021

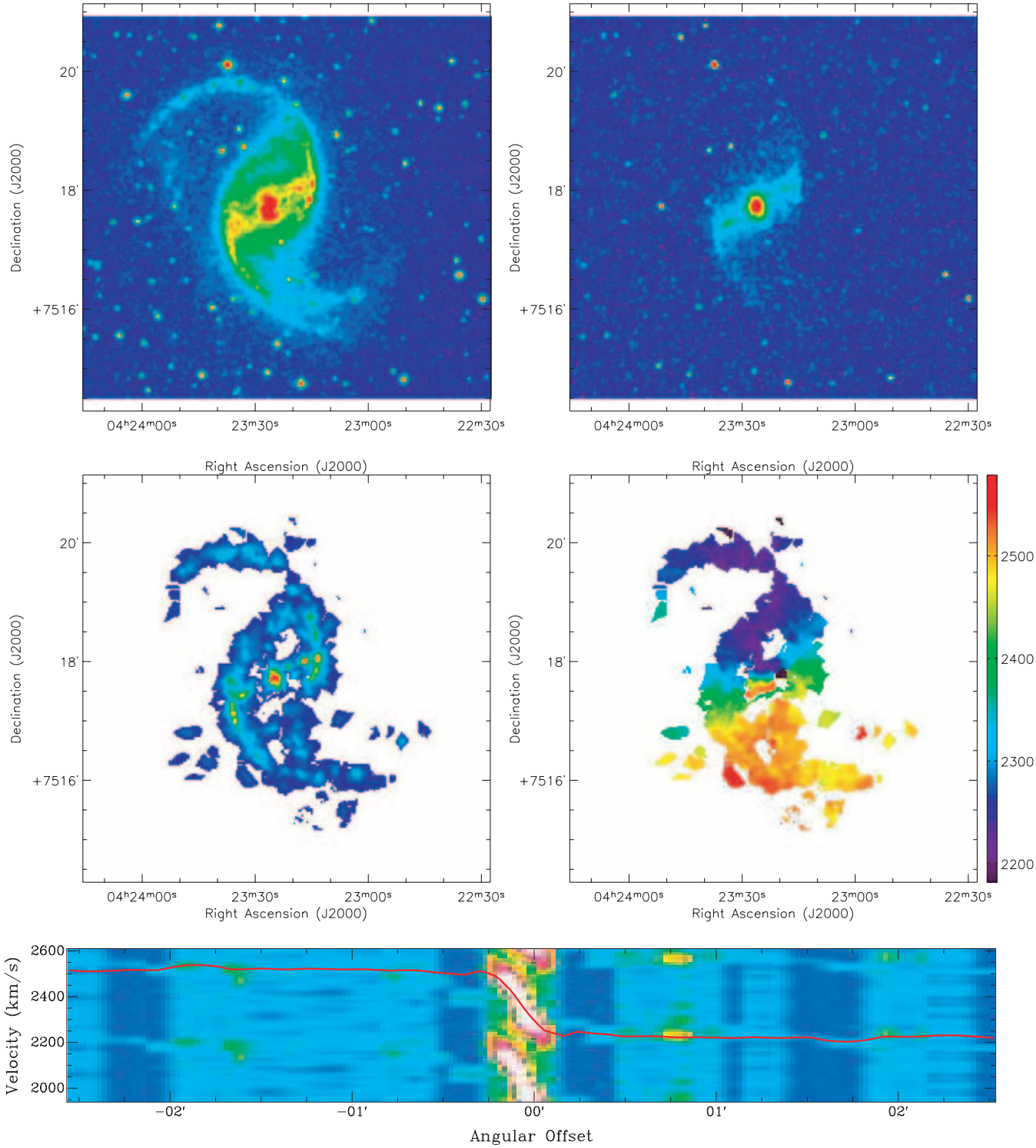

Figure 7. NGC 1530. Top left: XDSS blue-band image. Top right: 2MASS K_s-band image. Middle left: Hα monochromatic image. Middle right: Hα velocity field. Bottom: PV diagram.

galaxy is far from the calibration line, absolute values of the systemic velocity could be wrong (which is not a problem because we are mainly interested in relative velocities for our kinematical studies). In such cases, two ways are in development: a correction using the dispersion in the multilayer, semireflective high Finesse coating, which is hard to model for high multilayer coating, or/and an absolute calibration (in development) performed at the scanning wavelength. Nevertheless, the relative velocities with respect to the systemic velocity are very accurate, with an error of a fraction of a channel width (<3 km s^{-1}) over the whole field. In this study, systemic velocities of the sample, presented in Table 1, were taken directly from Tully (1988).

Downloaded from https://academic.oup.com/mnras/article/360/4/1201/1076455 by CNRS - ISTO user on 26 January 2021

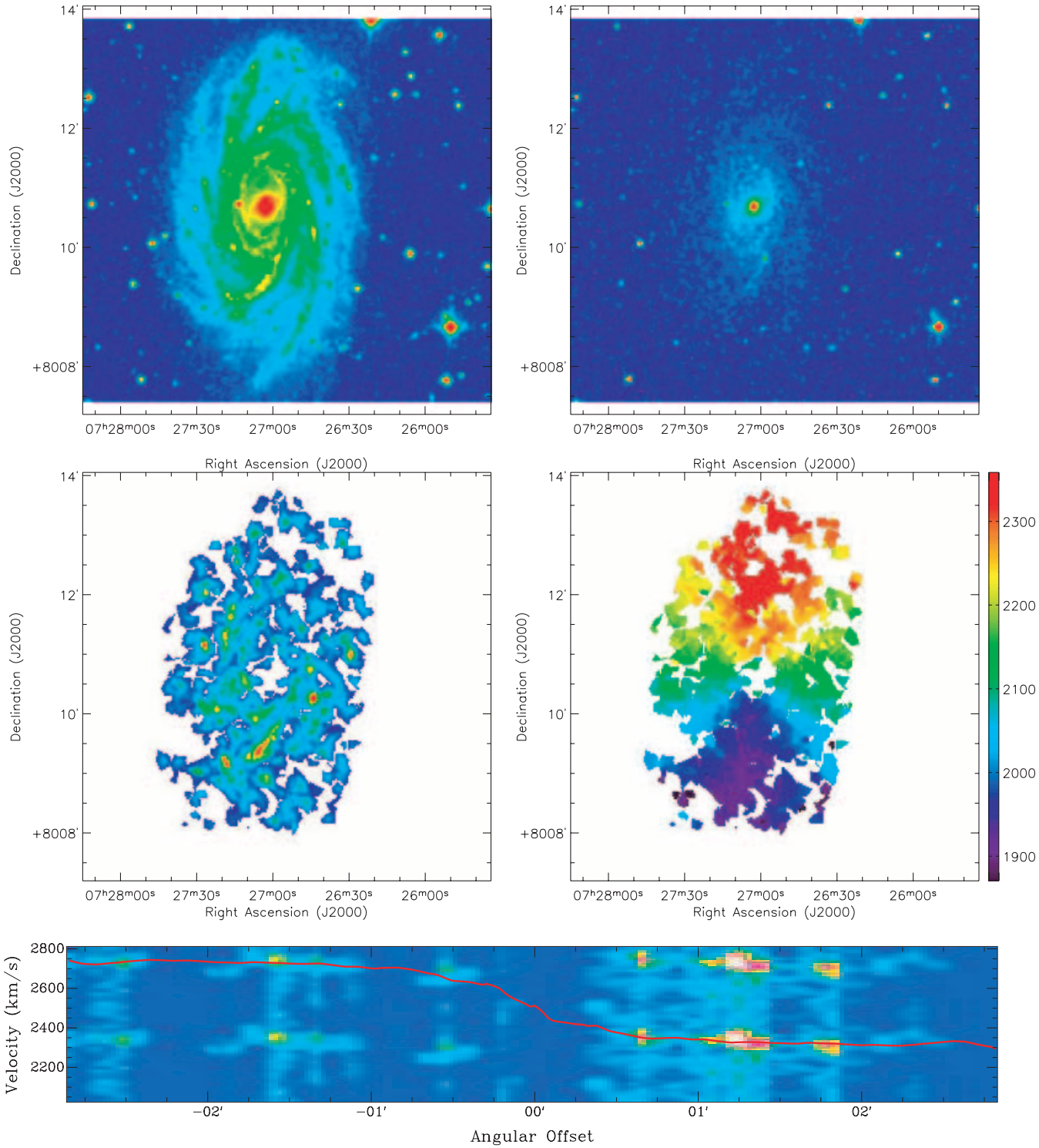

Figure 8. NGC 2336. Top left: XDSS blue-band image. Top right: 2MASS K_s-band image. Middle left: Hα monochromatic image. Middle right: Hα velocity field. Bottom: PV diagram.

The signal measured along the scanning sequence was separated in two parts: (i) an almost constant level produced by the continuum light in a narrow passband around Hα and (ii) a varying part produced by the Hα line (referred to hereafter as the monochromatic map). After this calibration step, an adaptive binning was performed.

3.2 Adaptive binning and maps

A Hanning smoothing was performed on all the data cubes along the spectral axis. The Hanning smoothing can suppress the problems connected with the frequency response (artefacts in the spectra caused by the sampling and the Fourier transform) of the spectra as

Downloaded from https://academic.oup.com/mnras/article/360/4/1201/1076455 by CNRS - ISTO user on 26 January 2021

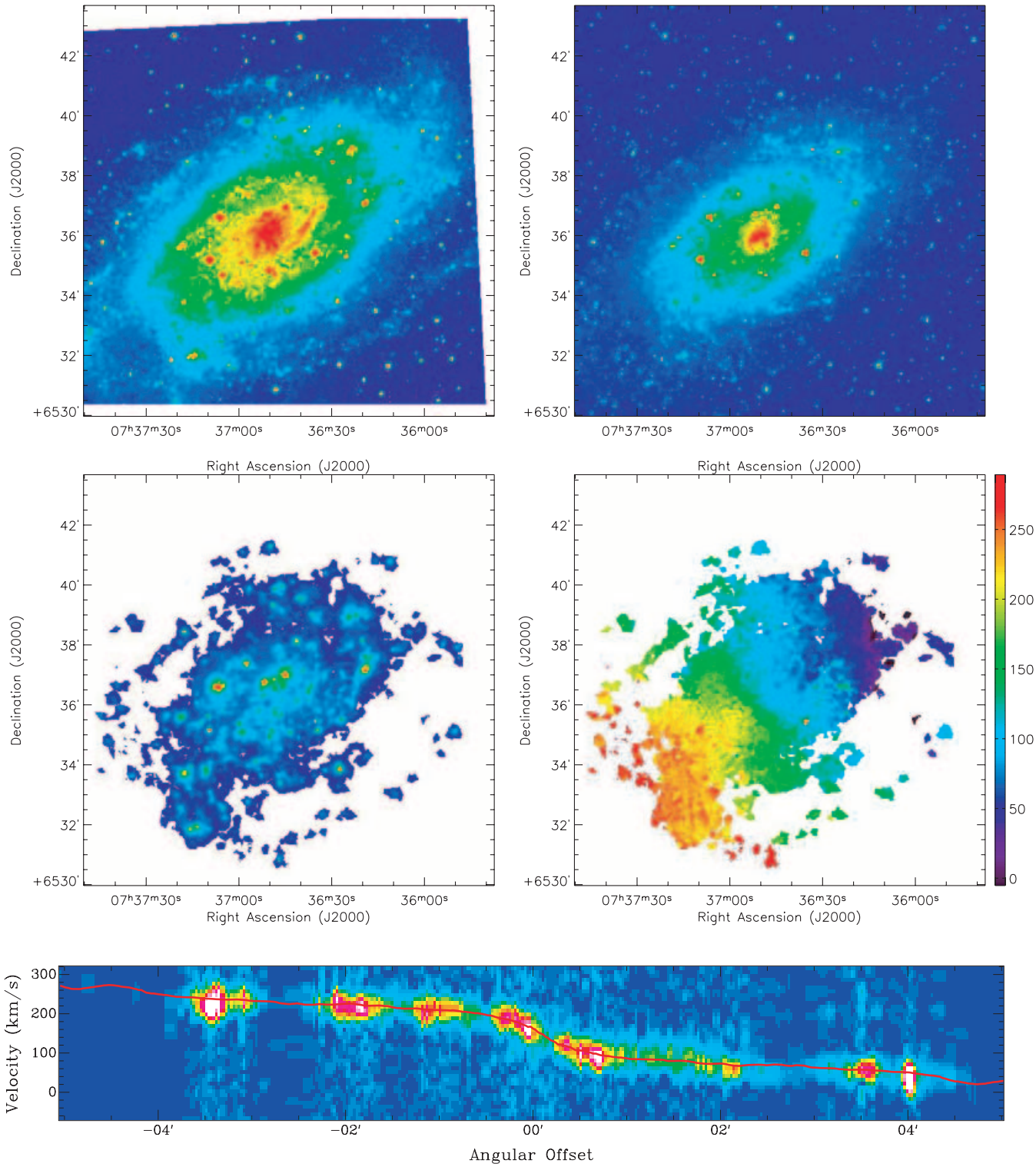

Figure 9. NGC 2403. Top left: XDSS blue-band image. Top right: 3.6-μm Spitzer image. Middle left: Hα monochromatic image. Middle right: Hα velocity field. Bottom: PV diagram.

a real function of finite length. The strong OH night sky lines passing through the filter were reconstructed into a cube and subtracted from the galaxy's spectrum (Daigle et al., in preparation).

In order to increase the S/N ratio, an adaptive spatial smoothing, based on the 2D-Voronoi tessellation method (Cappellari & Copin 2002) was also applied to the 3D data cubes (Daigle et al., in preparation) before producing the monochromatic images and velocity fields. Each pixel was binned to reach a S/N of typically 5–10, depending on the observation conditions and the morphological type of the galaxy. This clever smoothing is effective in low S/N regions.

Downloaded from https://academic.oup.com/mnras/article/360/4/1201/1076455 by CNRS - ISTO user on 26 January 2021

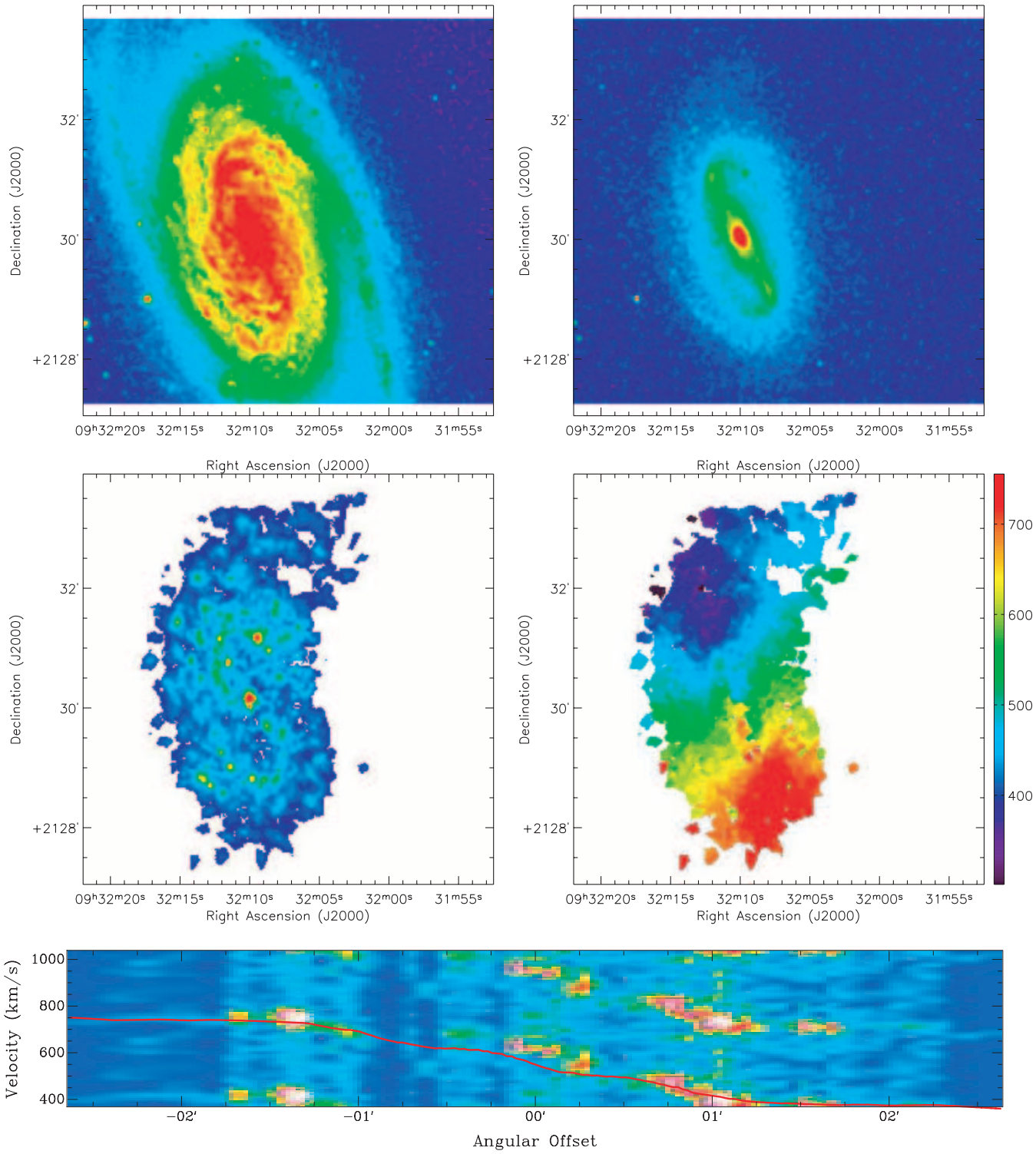

Figure 10. NGC 2903. Top left: XDSS blue-band image. Top right: 2MASS K_s-band image. Middle left: Hα monochromatic image. Middle right: Hα velocity field. Bottom: PV diagram.

First, in high S/N regions (S/N value superior to a fixed limit of 5, 7 or 10), the smoothing will not act and a bin is only one pixel. This will ensure we have the best spatial resolution possible in high S/N regions. This differs from the classical Gaussian smoothing (Garrido et al. 2003; Zurita et al. 2004) where the kernel used will perform the mix between a pixel and the adjacent one, and will cause a cross-pollution between the two regions. Secondly, for low S/N regions, pixels are binned until the S/N required is reached or the size of the resultant bin is reached (typically 30 pixel^2). This is very useful in interarm regions where the signal is dominated by the

Downloaded from https://academic.oup.com/mnras/article/360/4/1201/1076455 by CNRS - ISTO user on 26 January 2021

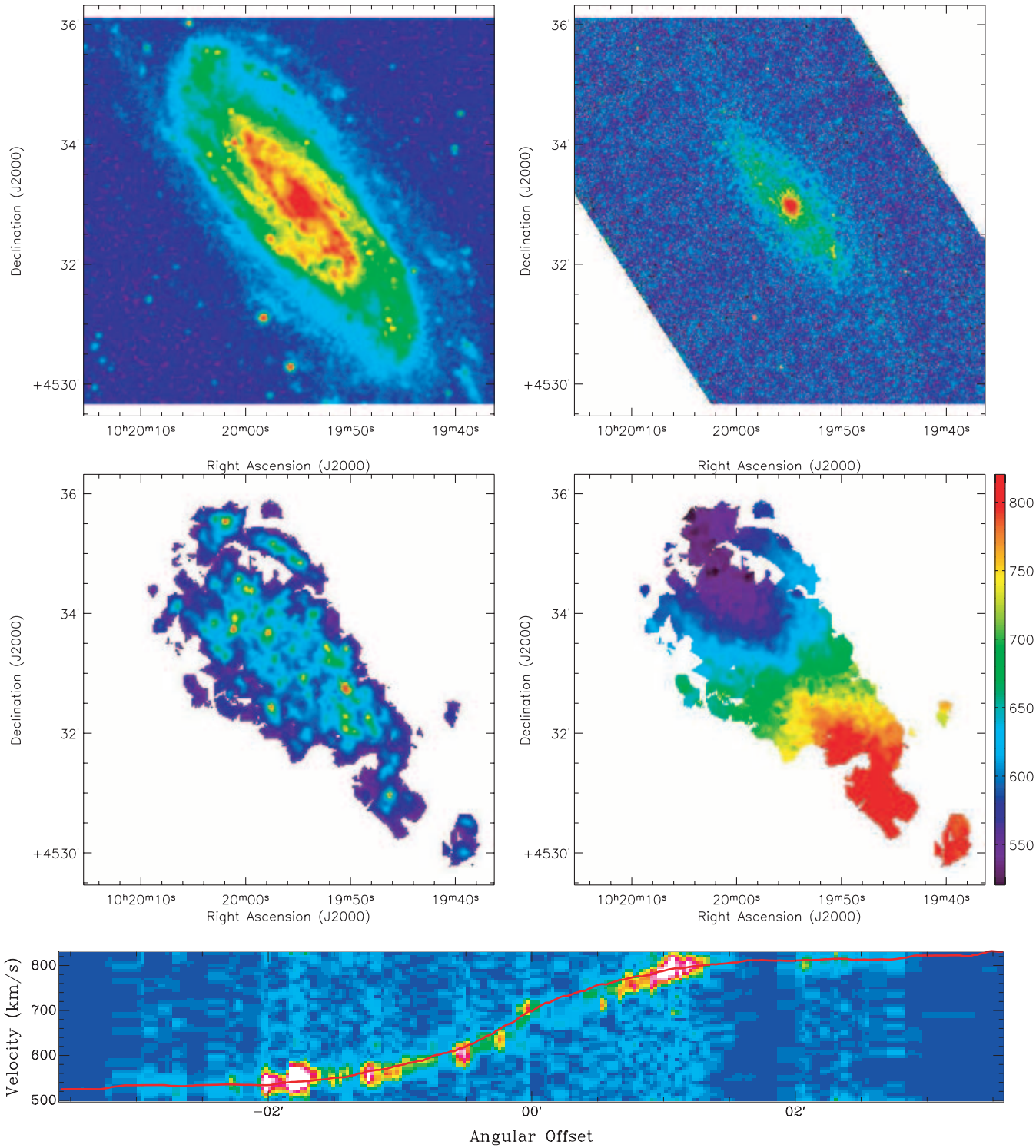

Figure 11. NGC 3198. Top left: XDSS blue-band image. Top right: 3.6-μm Spitzer image. Middle left: Hα monochromatic image. Middle right: Hα velocity field. Bottom: PV diagram.

diffuse Hα and not by H II regions. Thus, velocity maps have the best possible coverage without losing any spatial resolution in the high S/N regions.

Finally, the intensity-weighted mean (barycentre) of the Hα emission-line profile was converted into wavelength and then into heliocentric radial velocity. Monochromatic images were obtained by integrating the Hα profiles.

3.3 World Coordinate System astrometry

SAOIMAGE DS9, developed by the Smithsonian Astrophysical Observatory (Joye & Mandel 1999), has been used to find the correct astrometry of the monochromatic and Hα images. KARMA (Gooch 1996) and its routine KPVSLICE have been used to apply a coordinate system header to all images and data cubes. Systematic comparison

Downloaded from https://academic.oup.com/mnras/article/360/4/1201/1076455 by CNRS - ISTO user on 26 January 2021

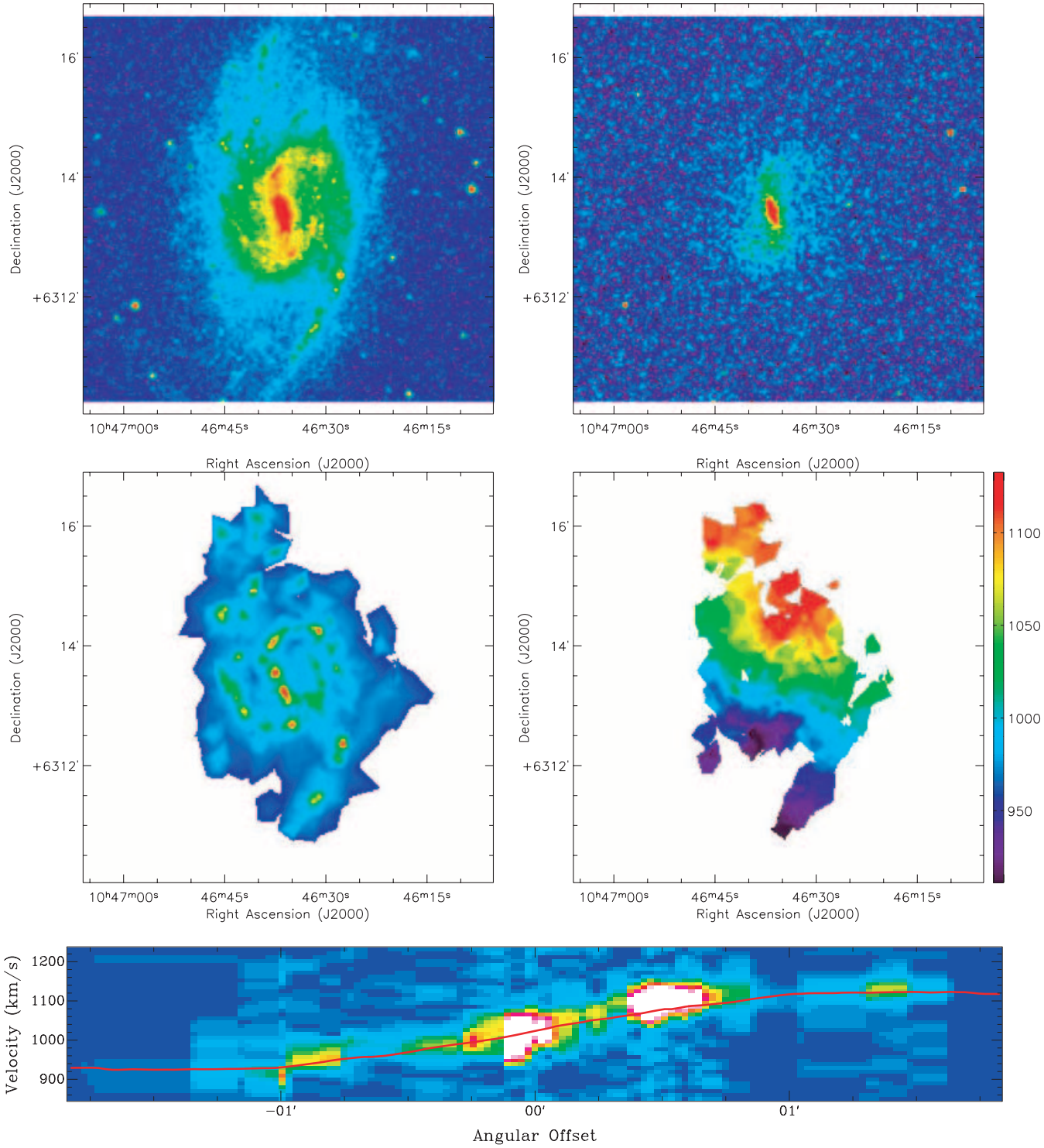

Figure 12. NGC 3359. Top left: XDSS blue-band image. Top right: 2MASS K_s-band image. Middle left: Hα monochromatic image. Middle right: Hα velocity field. Bottom: PV diagram.

between the K_s band and the XDSS blue-band images and the field stars in rough continuum images (with no adaptive binning) were made in order to find the correct WCS for each image. For the 21 galaxies of the BHαBAR sample, stars were easily found in rough continuum images.

4 DATA ANALYSIS

For each galaxy in the sample, Figs 5–25 provide: the blue-band image (XDSS or Knapen et al. 2004), the NIR image (SPITZER 3.6-μm, Knapen et al. 2003 or 2MASS image), the Hα

Downloaded from https://academic.oup.com/mnras/article/360/4/1201/1076455 by CNRS - ISTO user on 26 January 2021

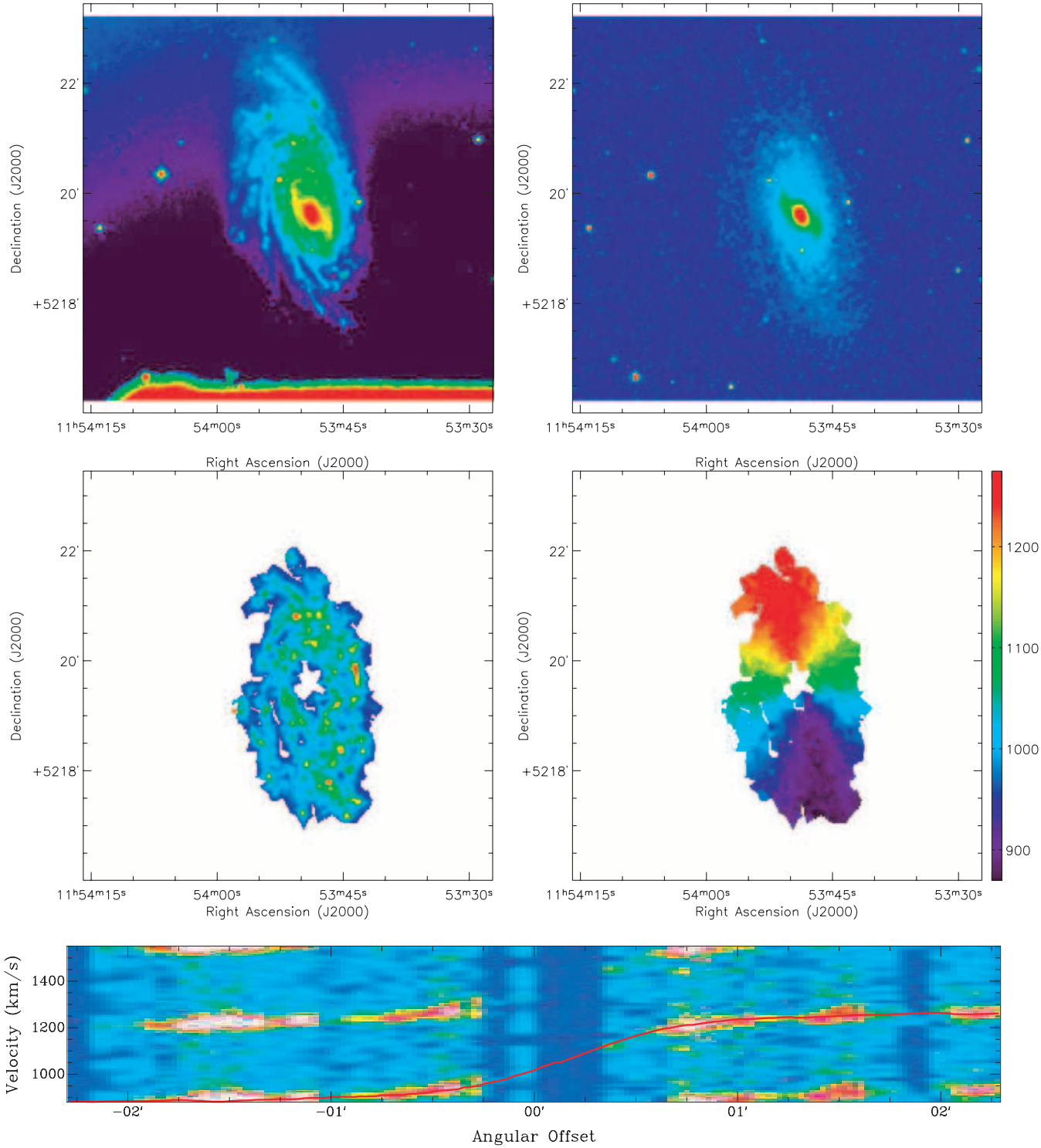

Figure 13. NGC 3953. Top left: XDSS blue-band image. Top right: 2MASS K_s-band image. Middle left: Hα monochromatic image. Middle right: Hα velocity field. Bottom: PV diagram.

monochromatic image, the velocity field and the position–velocity (PV) diagram.

Once the astrometry was performed on all the images and data cubes, the kinematical parameters were derived using GIPSY and KARMA.

The ROTCUR routine in the GIPSY package was used to find the kinematical parameters of the galaxies studied. ROTCUR (Begeman 1987) derives the kinematical parameters from the observed velocity field by fitting tilted-ring models. The observed velocities given in the velocity maps, $V_{\rm obs}$, are obtained by solving the following

Downloaded from https://academic.oup.com/mnras/article/360/4/1201/1076455 by CNRS - ISTO user on 26 January 2021

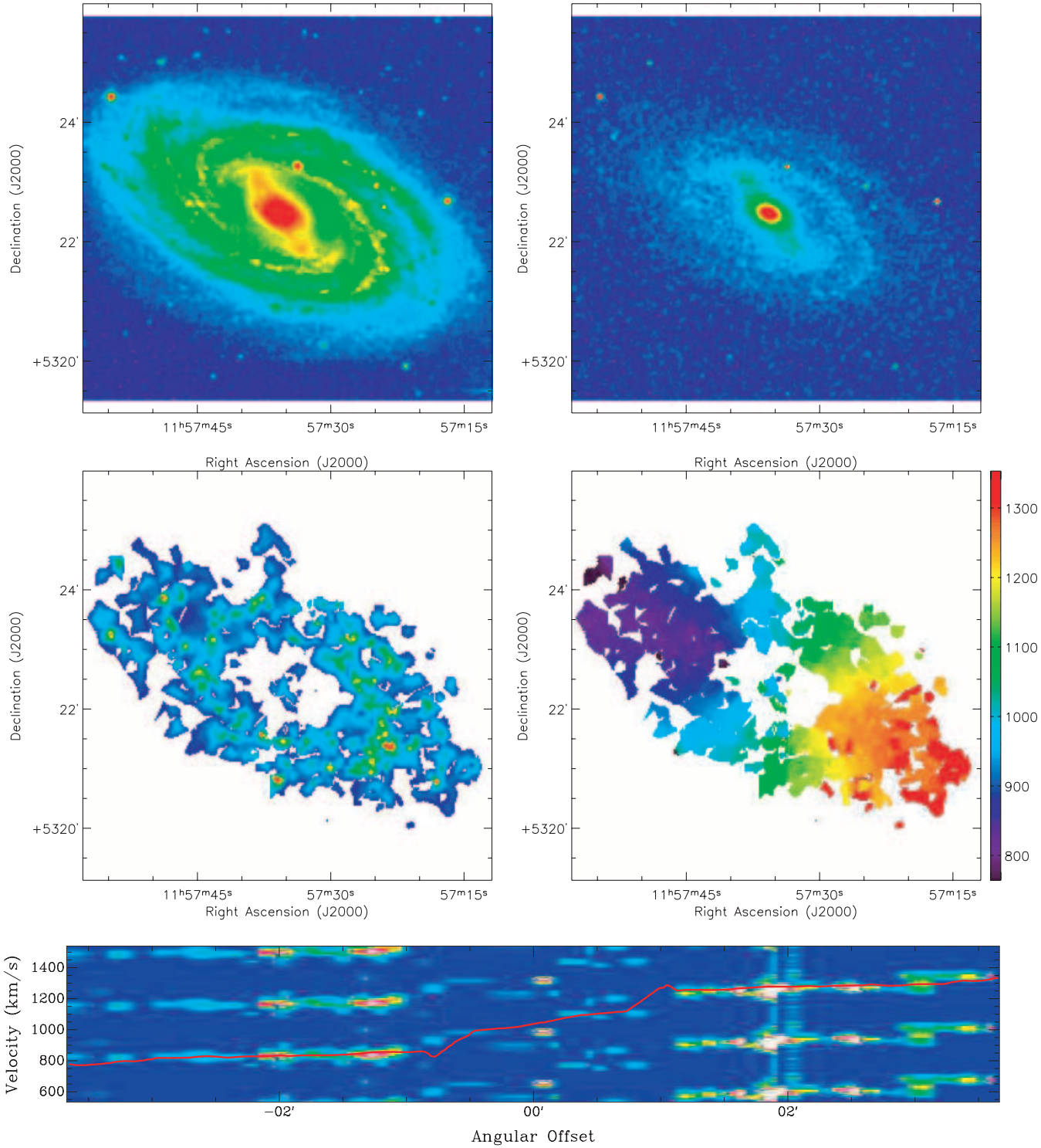

Figure 14. NGC 3992. Top left: XDSS blue-band image. Top right: 2MASS K_s-band image. Middle left: Hα monochromatic image. Middle right: Hα velocity field. Bottom: PV diagram.

equation

$$V_{\rm obs} = V_{\rm sys} + V_{\rm rot}(R)\cos\theta\sin i + V_{\rm exp}(R)\sin\theta\sin i,$$

where $V_{\rm rot}$ is the rotation velocity, $V_{\rm exp}$ is the expansion velocity, R and θ are the polar coordinates in the plane of the galaxy and i is the inclination. The same procedure was used for all the galaxies in the sample. In order to have a good sampling of the signal, the physical width of the rings is always the same: 4.83 arcsec for the OmM, 2.04 arcsec for the OHP and 1.44 arcsec for the CFHT data.

Because all the galaxies in the BHαBAR sample are barred, it was decided to derive the kinematical parameters only in the

Downloaded from https://academic.oup.com/mnras/article/360/4/1201/1076455 by CNRS - ISTO user on 26 January 2021

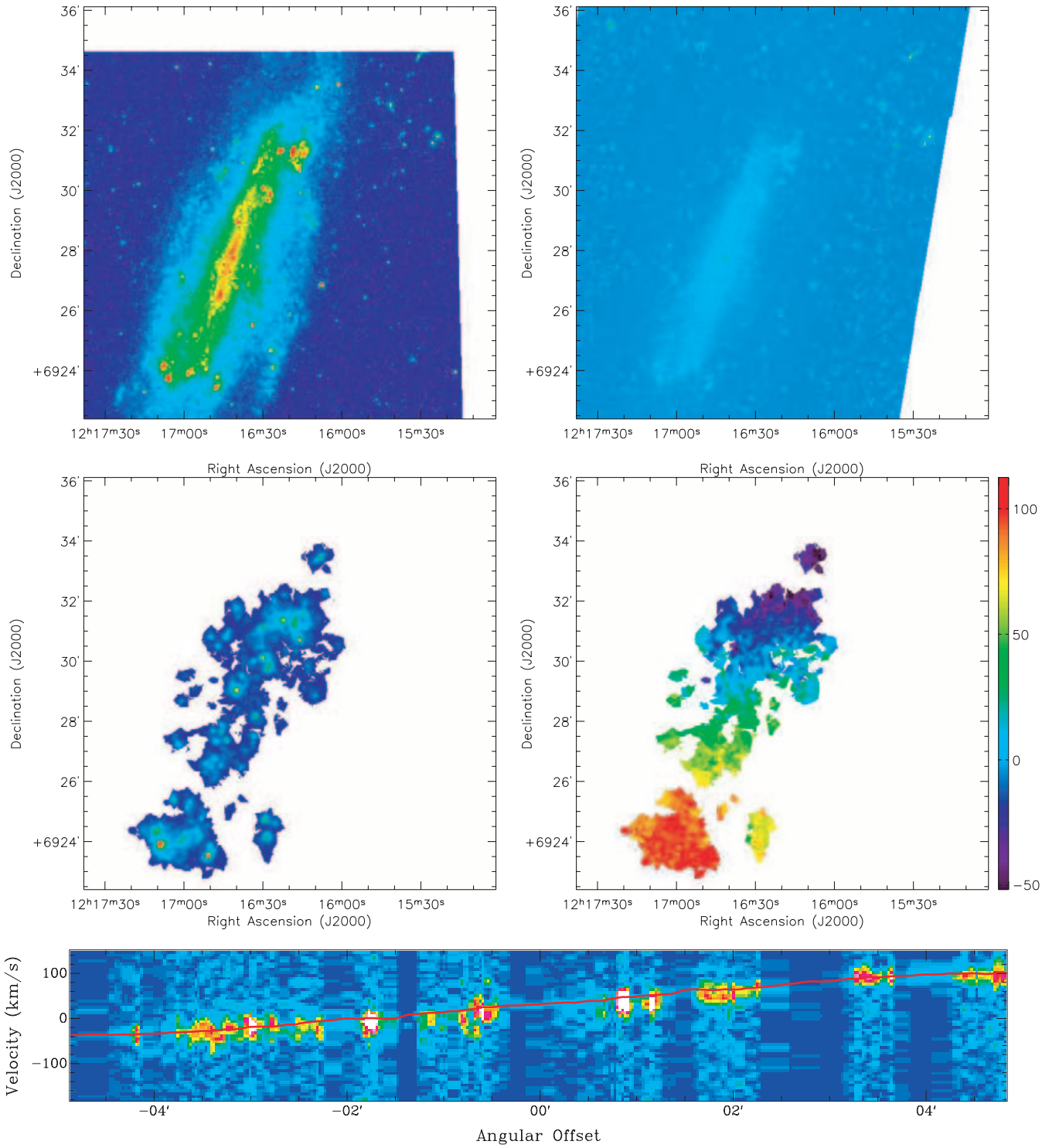

Figure 15. NGC 4236. Top left: XDSS blue-band image. Top right: 3.6-μm Spitzer image. Middle left: Hα monochromatic image. Middle right: Hα velocity field. Bottom: PV diagram.

axisymmetric part of the disc of the galaxy. This means that the central regions of the galaxy were systematically masked to avoid contamination from non-circular motions due to the presence of the bar. Obviously, the solution will still be affected by the non-circular motions of the spiral disc itself. In order to determine the range of galactic radii to apply ROTCUR, we used the values of the deprojected bar lengths given by Martin (1995), and reported in Table 1, column 9. For five galaxies not belonging to the 'Martin' sample (IC 0342, NGC 1530, NGC 2403, 4535 and 5964), an ellipse fitting was carried out to determine an approximate bar length.

For each galaxy in the sample, a fit is first done simultaneously for the kinematical centre ($x_{\rm pos}$, $y_{\rm pos}$) and the systemic velocity

Downloaded from https://academic.oup.com/mnras/article/360/4/1201/1076455 by CNRS - ISTO user on 26 January 2021

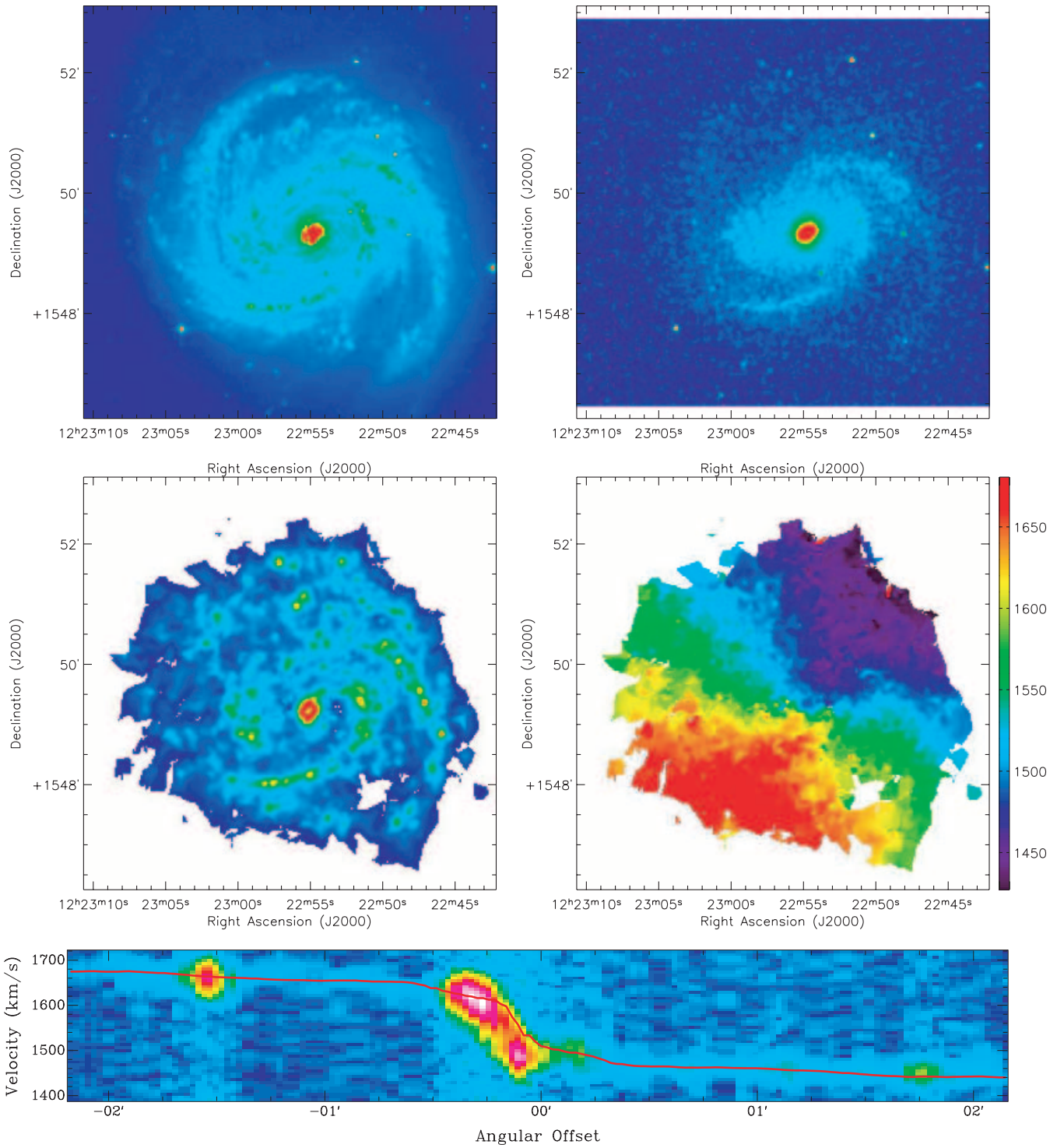

Figure 16. NGC 4321. Top left: *B*-band image from Knapen et al. (2004). Top right: 3.6-μm Spitzer image. Middle left: Hα monochromatic image. Middle right: Hα velocity field. Bottom: PV diagram.

V_{sys}, fixing the position angle (PA) and the inclination i (using the photometrical values).

Secondly, by keeping V_{sys} and the kinematical centre fixed, PA and i are allowed to vary over the same radius range and their mean values derived. It was decided to use the mean values of PA and i because discs are rarely warped inside the optical radius; warps are mainly seen for $R > R_{opt}$. Then V_{rot} are calculated keeping the five derived kinematical parameters, (x_{pos}, y_{pos}), V_{sys}, PA and i, fixed over the whole radius range. In all the fits, V_{exp} was not considered and fixed to zero. Finally, a 2D kinematical model for each galaxy of the BHαBAR sample was constructed using the VELFI routine of GIPSY and subtracted from the data to obtain a residual velocity map. This whole process was repeated until the mean and the dispersion of residuals were found to be minimal and close to zero

Downloaded from https://academic.oup.com/mnras/article/360/4/1201/1076455 by CNRS - ISTO user on 26 January 2021

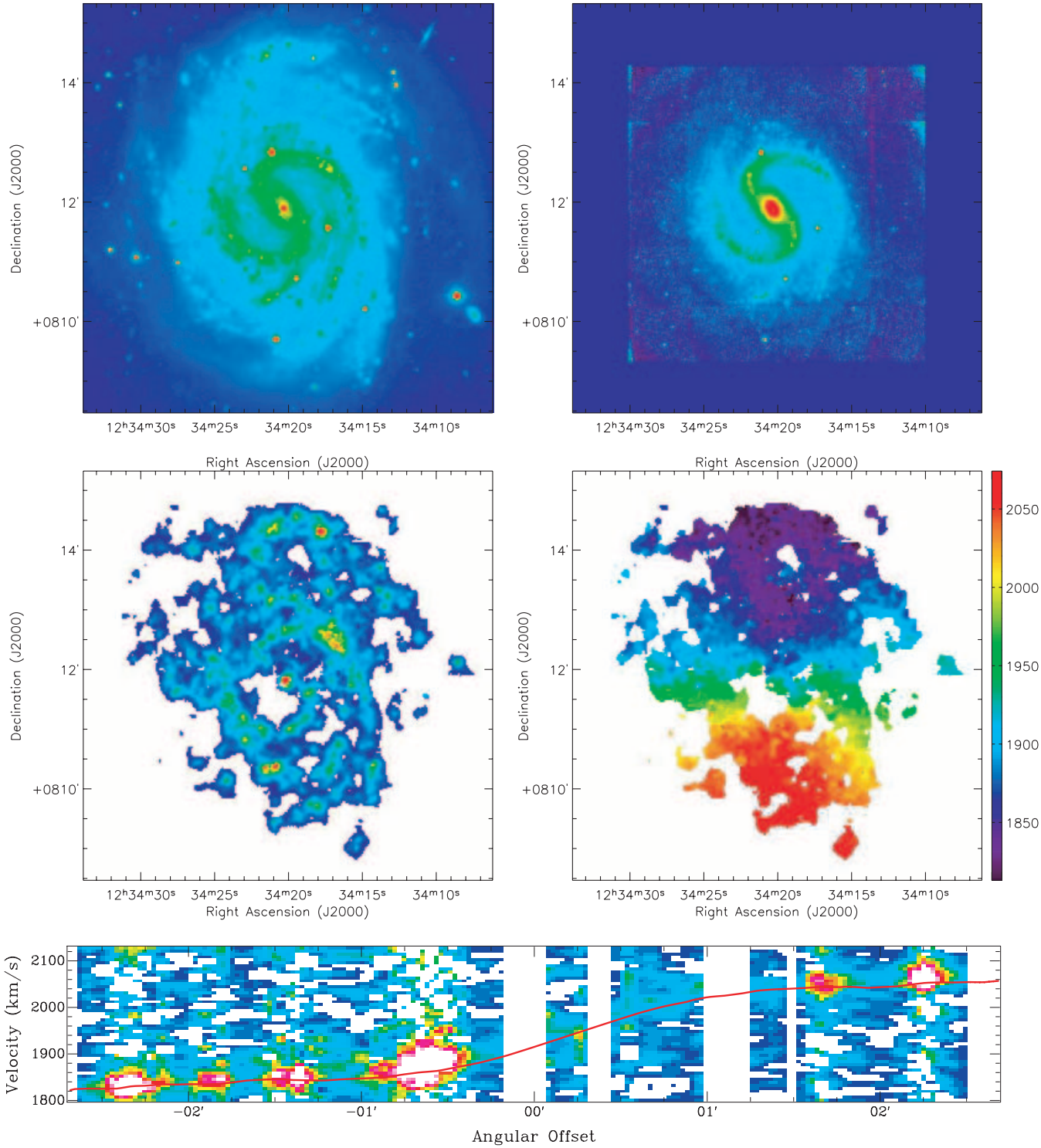

Figure 17. NGC 4535. Top left: *B*-band image from Knapen et al. (2004). Top right: K_s-band image from Knapen et al. (2003). Middle left: Hα monochromatic image. Middle right: Hα velocity field. Bottom: PV diagram.

and with a distribution as homogeneous as possible over the whole FOV.

To quantify the effect of masking the bar in the determination of the disc parameters, the residual maps (including the bar and masking it) were systematically compared. The means and the dispersions were computed for each residual map and for each galaxy. Results are presented in Table 4. The differences between the mean of the residual map in the disc part, using the model with the bar, and the mean of the residual map in the disc part, using the model avoiding the bar, are always close to zero (except for NGC 7479, where there is a severe perturbation in the western arm). A difference is noticeable when comparing the dispersion of the residuals

Downloaded from https://academic.oup.com/mnras/article/360/4/1201/1076455 by CNRS - ISTO user on 26 January 2021

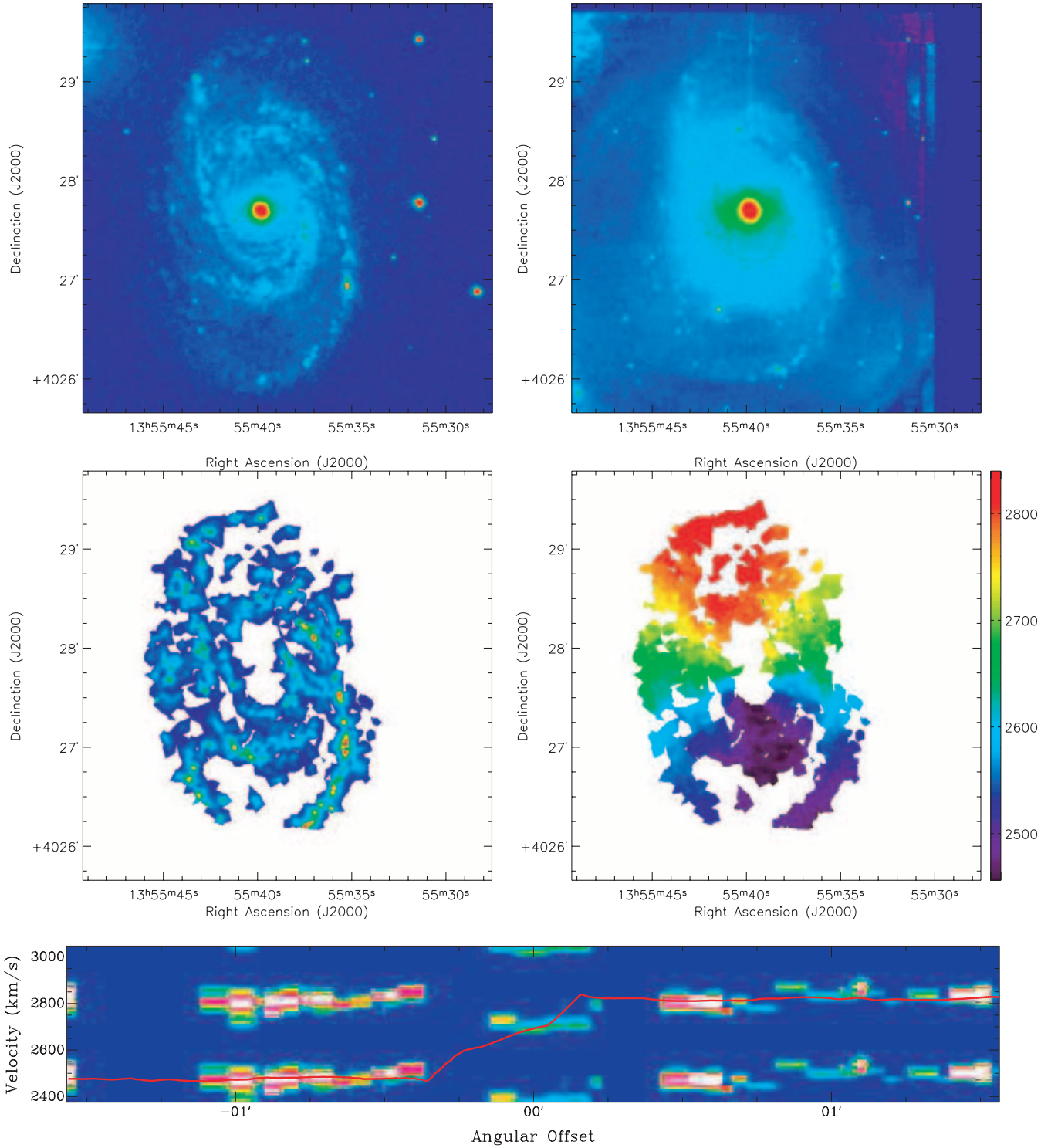

Figure 18. NGC 5371. Top left: *B*-band image from Knapen et al. (2004). Top right: K_s-band image from Knapen et al. (2003). Middle left: Hα monochromatic image. Middle right: Hα velocity field. Bottom: PV diagram.

in the disc part, using the model with the bar, and the dispersion of the residuals in the disc part, using the model avoiding the bar. The latter is always smaller than the former (<20 km s^{-1}). This suggests that the determination of the disc parameters is better when the bar region is avoided.

Once the most suitable 2D kinematical model was found, the KPVSLICE routine of KARMA was used to derive a PV diagram. This PV diagram is useful to check if the RC derived from the whole 2D velocity field is a good representation of the kinematics on the major axis. As the axisymmetrical models were derived using the disc region avoiding the bar, it is clear that strong non-axisymmetrical motions can be seen in the bar region (e.g. NGC 0925, 2903, 3198, 3359, 6217 and 7741). When the range of velocities in a galaxy was superior to the free spectral range of the

Downloaded from https://academic.oup.com/mnras/article/360/4/1201/1076455 by CNRS - ISTO user on 26 January 2021

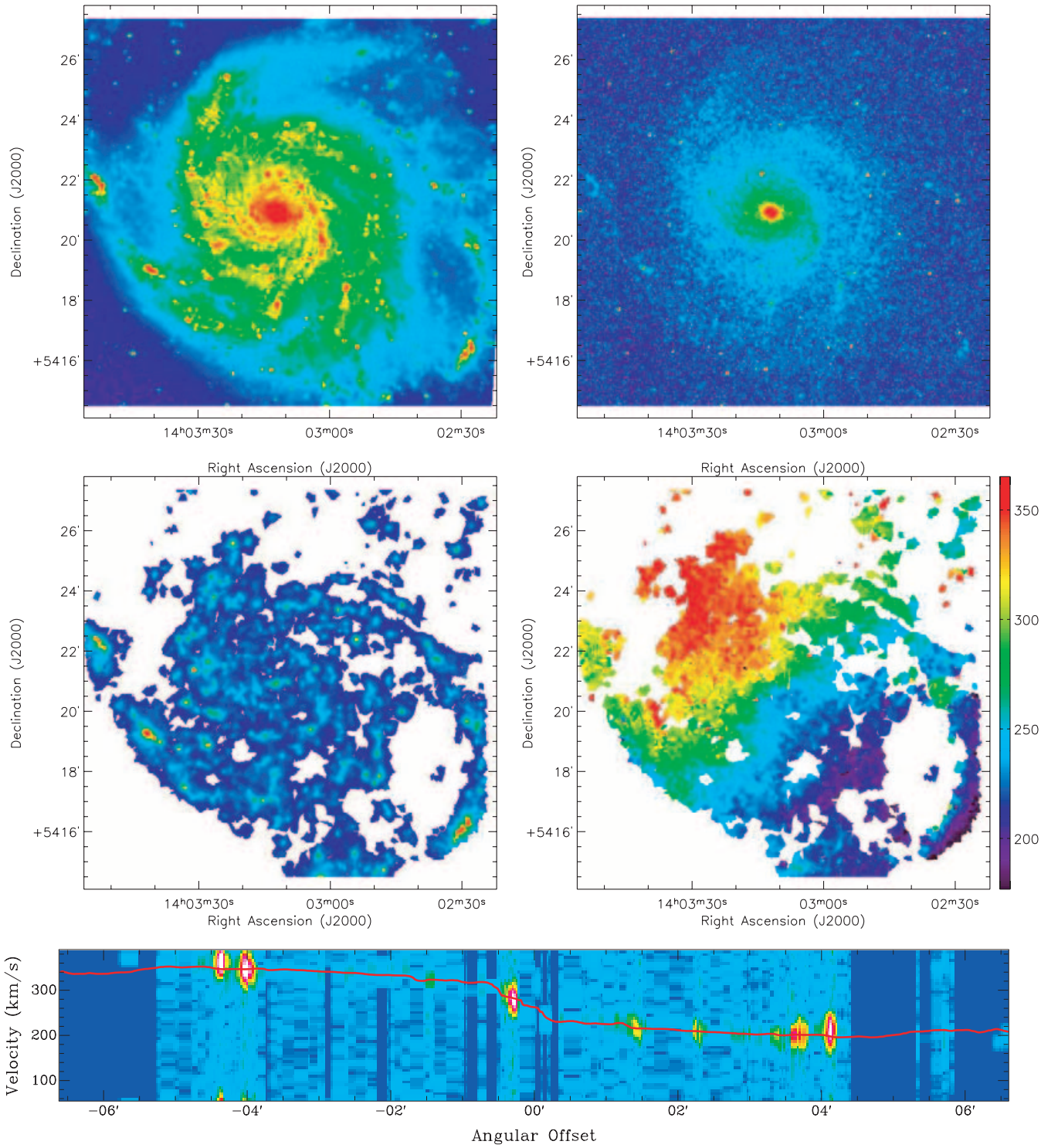

Figure 19. NGC 5457. Top left: XDSS blue-band image. Top right: 2MASS K_s-band image. Middle left: Hα monochromatic image. Middle right: Hα velocity field. Bottom: PV diagram.

etalon used, the overall velocity range was distributed over two or three orders. In this case, data cubes have been replicated in the spectral dimension (two or three times) to construct the PV diagrams. This is the case for NGC 7479, 5371, 4535, 3992, 3953, 2903, 2336 and 1530.

Table 5 gives the results for the kinematical parameter fitting, compares with the photometrical data of the RC3 and indicates the shift between the photometrical and kinematical centres. Because, in the ROTCUR task, the kinematical value of the PA is defined as the angle measured counterclockwise from the north to the receding side of the velocity field, it may thus differ from the RC3 value by 180°.

The agreement is good between the photometrical and the kinematical PA, even for low inclination galaxies for which the

Downloaded from https://academic.oup.com/mnras/article/360/4/1201/1076455 by CNRS - ISTO user on 26 January 2021

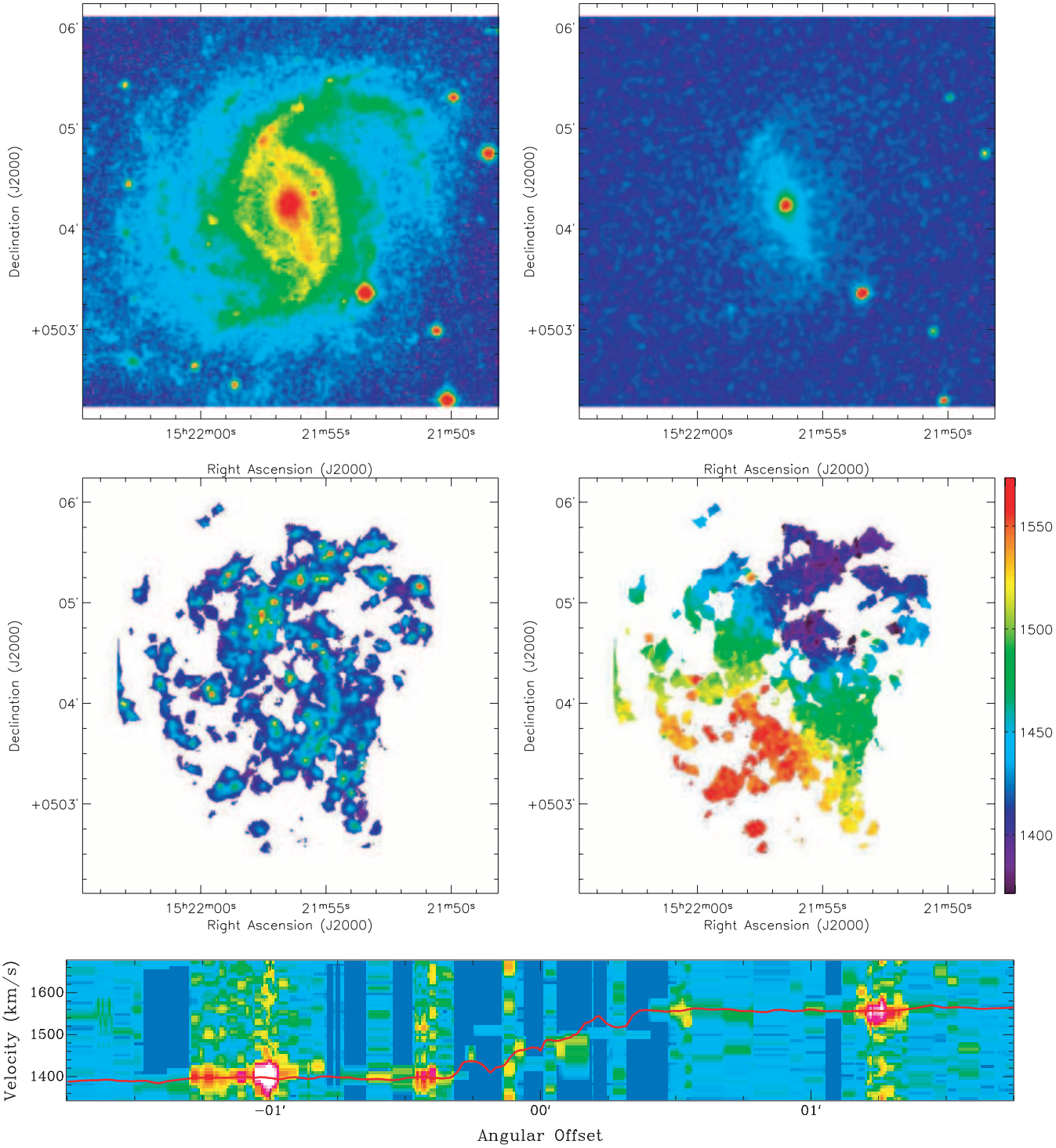

Figure 20. NGC 5921. Top left: XDSS blue-band image. Top right: 2MASS K_s-band image. Middle left: Hα monochromatic image. Middle right: Hα velocity field. Bottom: PV diagram.

photometrical position angle is difficult to determine accurately (Fig. 3, left).

When comparing inclinations, noticeable discrepancies can be seen for two galaxies having a round shape (IC 0342 and NGC 4321) and a low photometrical inclination (<20°). The photometrical method used to determine the inclination, by fitting ellipses to the outer isophotes (or simply from the axis ratios), minimizes the inclination while the kinematical method is much less sensitive to this 'face-on' effect. The shift between the position of the centre of the galaxy determined from the photometry and the kinematics is clearly a function of the morphological type of the galaxy (see Fig. 4). The strongest discrepancies occur for later-type spirals for which the photometrical centre is not always easy to identify. The large value of the offset when plotted in units of arcsec

Downloaded from https://academic.oup.com/mnras/article/360/4/1201/1076455 by CNRS - ISTO user on 26 January 2021

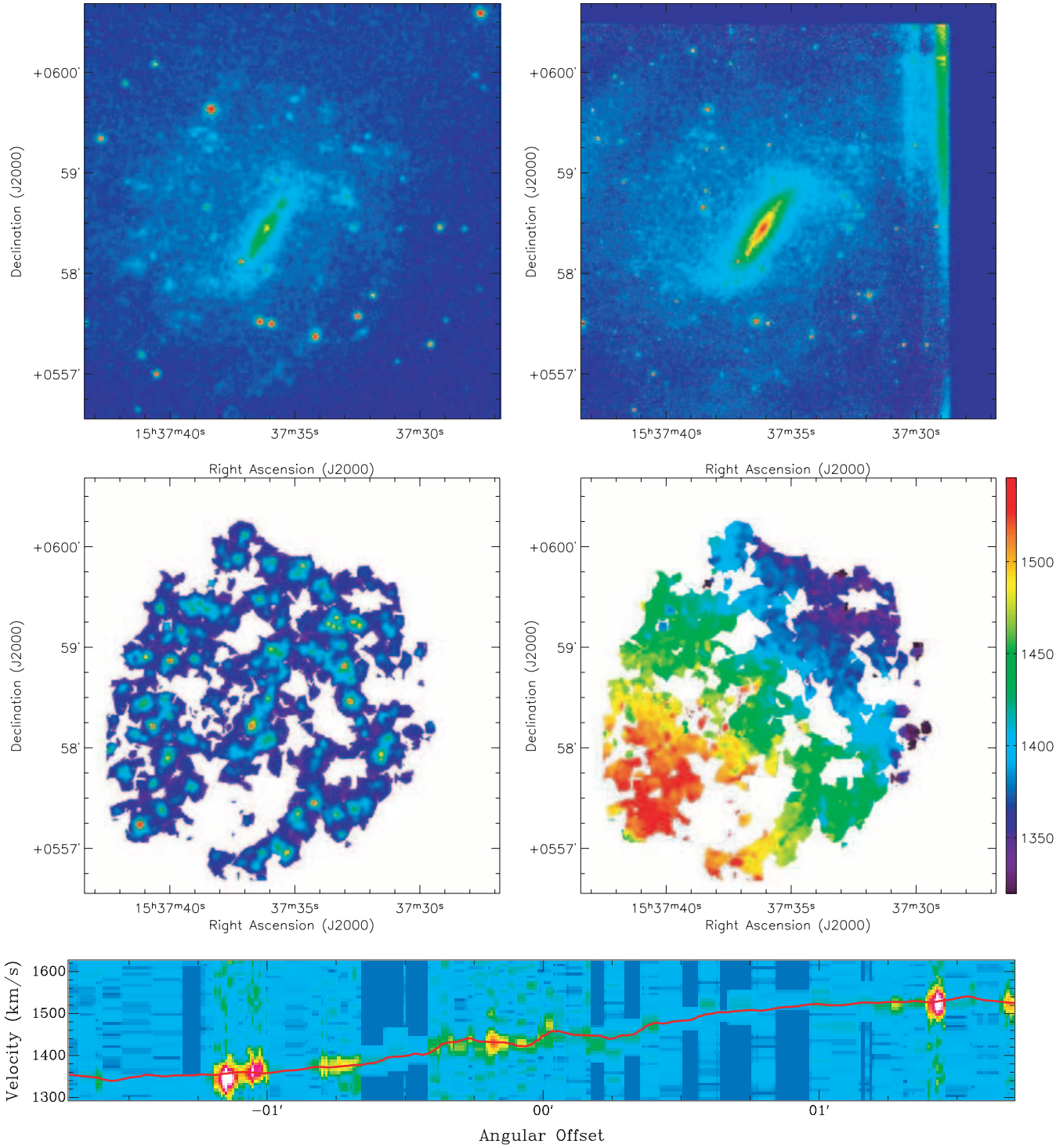

Figure 21. NGC 5964. Top left: *B*-band image from Knapen et al. (2004). Top right: K_s-band image from Knapen et al. (2003). Middle left: Hα monochromatic image. Middle right: Hα velocity field. Bottom: PV diagram.

in Fig. 4 (left panel) shows that, for a large majority of galaxies, this difference may not be explained by seeing or spatial resolution effects. On the other hand, this offset is not statistically significant: NGC 2403, IC 0342, NGC 0925 and 5457 have offsets of 1.17, 0.89, 0.67 and 0.30 kpc, respectively, while the bulk of 15 galaxies out of 19 has an offset lower or equal to 0.1 kpc (Note that only 19 galaxies out of 21 were studied because the determination of the photometrical centre for NGC 4236 and 5964 was too hazardous).

Future *N*-body models coupled to an SPH code will help understand the gas behaviour in a non-axisymmetrical potential and may provide an explanation for such differences. The full analysis will be presented later.

Downloaded from https://academic.oup.com/mnras/article/360/4/1201/1076455 by CNRS - ISTO user on 26 January 2021

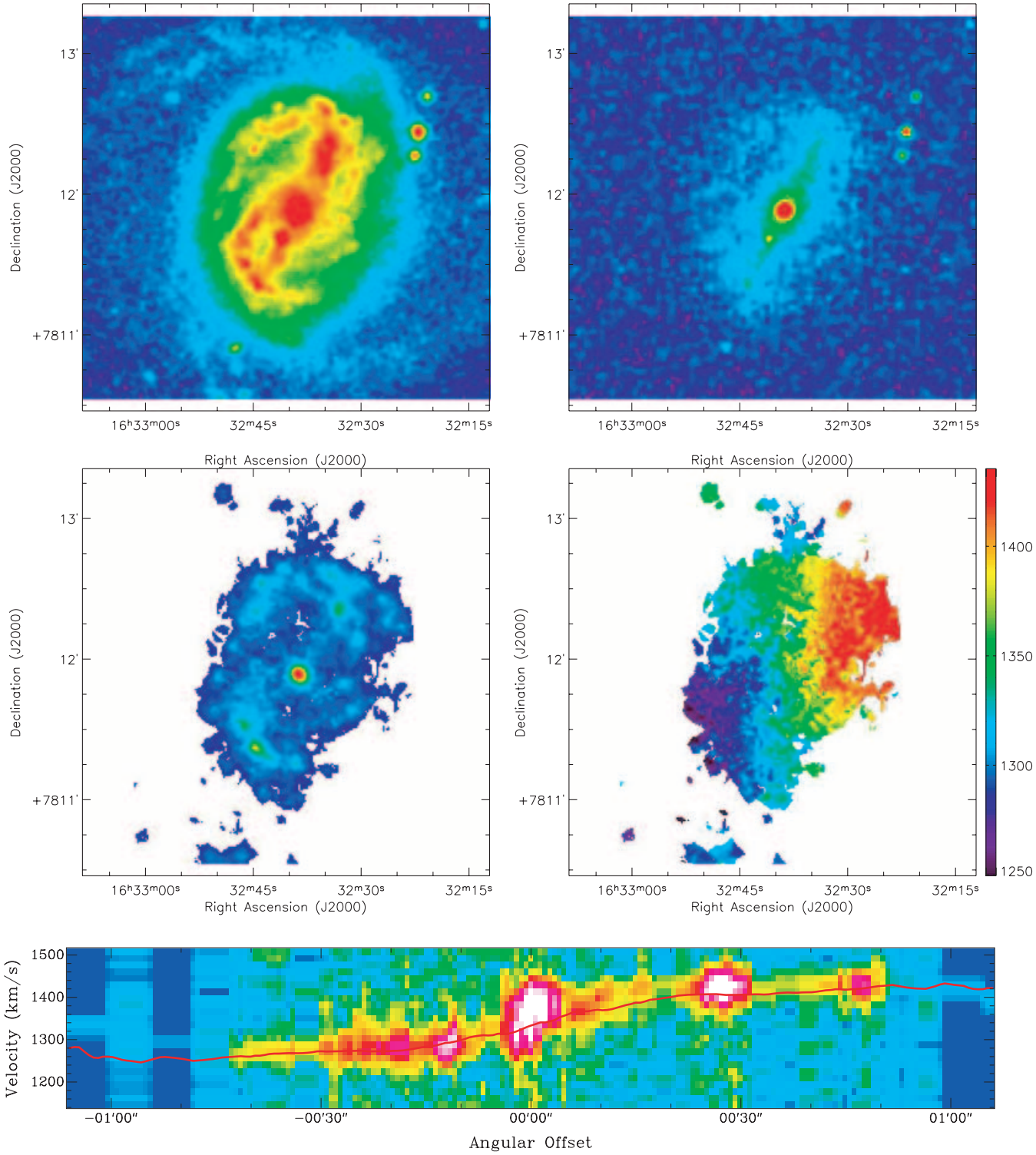

Figure 22. NGC 6217. Top left: XDSS blue-band image. Top right: 2MASS K_s-band image. Middle left: Hα monochromatic image. Middle right: Hα velocity field. Bottom: PV diagram.

5 CONCLUDING REMARKS AND FURTHER WORK

The 3D data presented in this paper are the results of a survey of the Hα kinematics of nearby barred galaxies with the FP integral-field spectrometer FaNTOmM. This study provides a homogeneous sample of barred galaxies. The 3D data were processed through a robust reduction pipeline. An adaptive binning method has been used to achieve optimal spatial coverage and resolution at a given S/N ratio, typically around 7. High spatial and spectral resolution Hα monochromatic maps and velocity fields are presented. Bar signatures in velocity fields and PV diagrams reveal strong non-circular motions and thus provide observational constraints to

Downloaded from https://academic.oup.com/mnras/article/360/4/1201/1076455 by CNRS - ISTO user on 26 January 2021

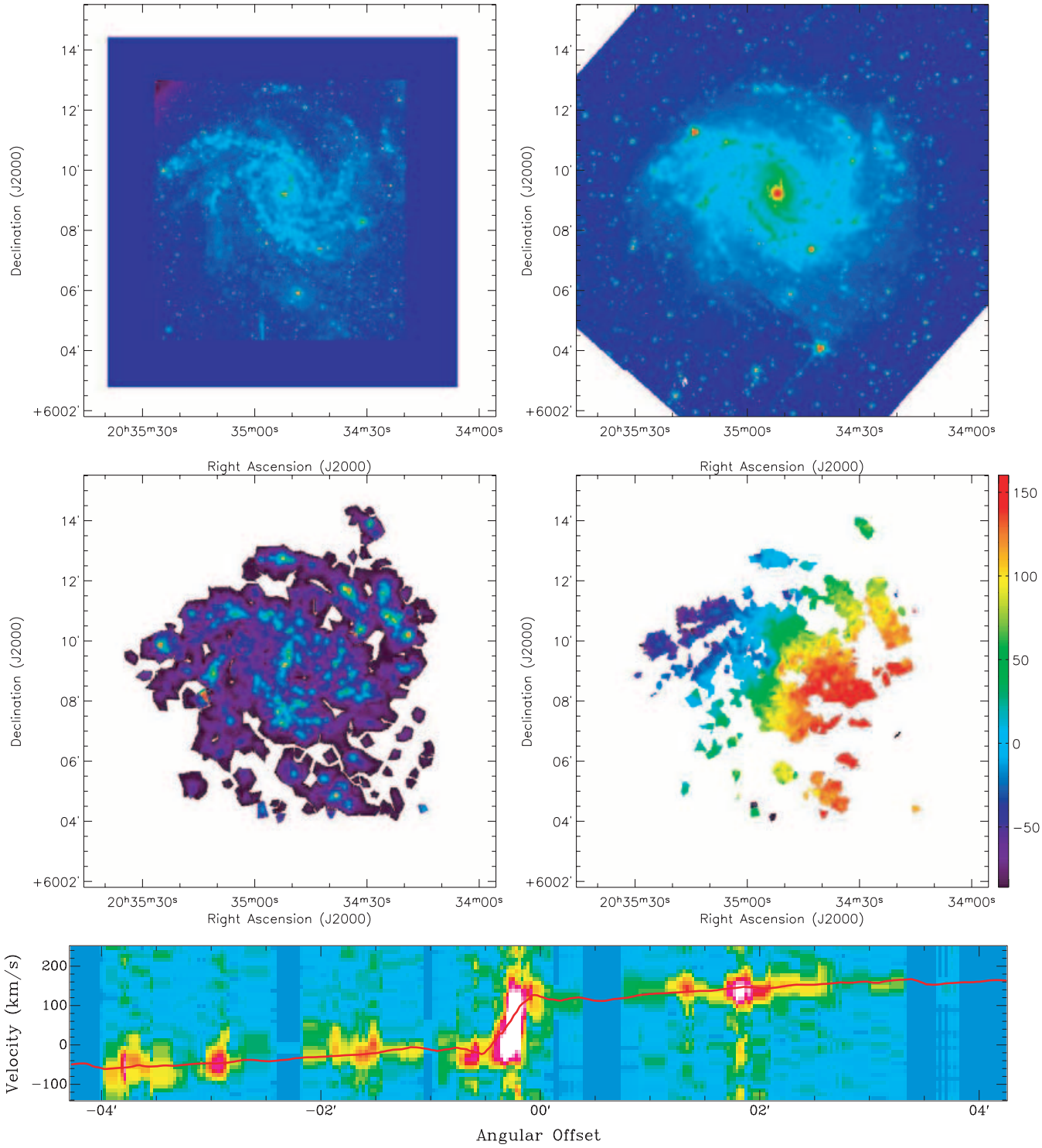

Figure 23. NGC 6946. Top left: *B*-band image from Knapen et al. (2004). Top right: 3.6-μm Spitzer image. Top right: 2MASS K_s-band image. Middle left: Hα monochromatic image. Middle right: Hα velocity field. Bottom: PV diagram.

extract the parameters of the bar and of the disc. Fine tuning of PAs and inclinations has been carried out. The kinematical parameters have been determined using a tilted-ring model, by taking into account only the axisymmetric part of the disc to avoid any kind of contamination due to non-circular motions from the bar (in the inner parts of the disc) or to a possible warp (in the outer parts).

The analysis of the sample shows that the photometrical and kinematical parameters (PA of the major axis, inclination and centre) are in relative good agreement, except perhaps for the later-type spirals. Nevertheless, the determination of the kinematical parameters is more accurate than the photometrical one.

The main purpose of the paper is to provide and present a homogeneous 3D data sample of nearby barred galaxies useful for further

Downloaded from https://academic.oup.com/mnras/article/360/4/1201/1076455 by CNRS - ISTO user on 26 January 2021

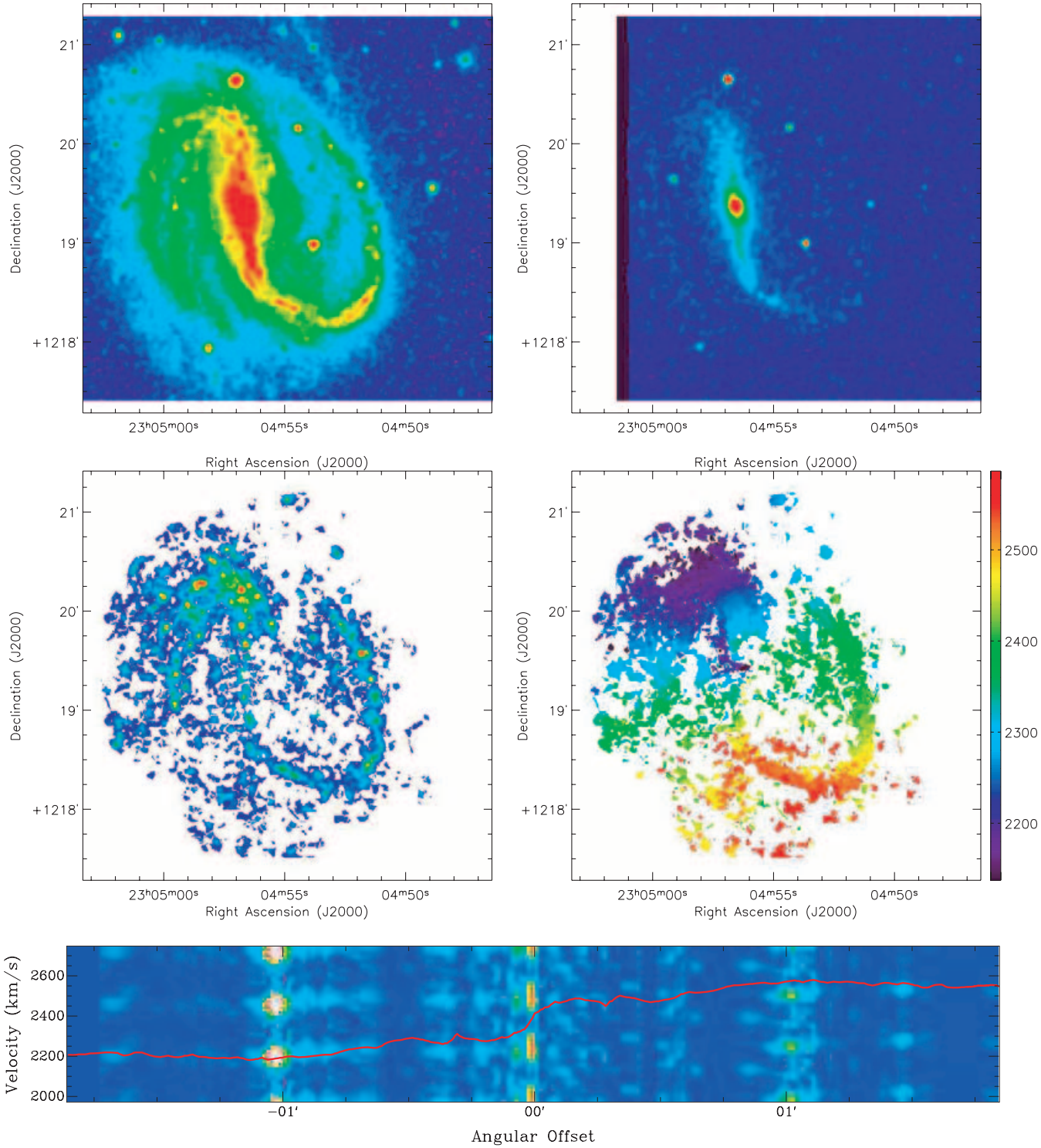

Figure 24. NGC 7479. Top left: XDSS blue-band image. Top right: 2MASS K_s-band image. Middle left: Hα monochromatic image. Middle right: Hα velocity field. Bottom: PV diagram.

analysis. Velocity patterns of the bar(s) and of the spiral will be accurately determined using the Tremaine–Weinberg method (Tremaine & Weinberg 1984) on the Hα velocity fields in two forthcoming papers. In Paper II, the Tremaine–Weinberg method applied to the gaseous component will be discussed using numerical simulations and illustrated with the galaxy M100. In Paper III, the rest of the sample will be analysed using this Tremaine–Weinberg method. In Paper IV, the RCs will be derived, properly corrected for non-circular motions in order to retrieve the actual mass distributions. This will be achieved with N-body coupled with SPH simulations for each velocity fields of the BHαBAR sample. This type of approach has been recently used by Pérez, Fux & Freeman (2004). However,

Downloaded from https://academic.oup.com/mnras/article/360/4/1201/1076455 by CNRS - ISTO user on 26 January 2021

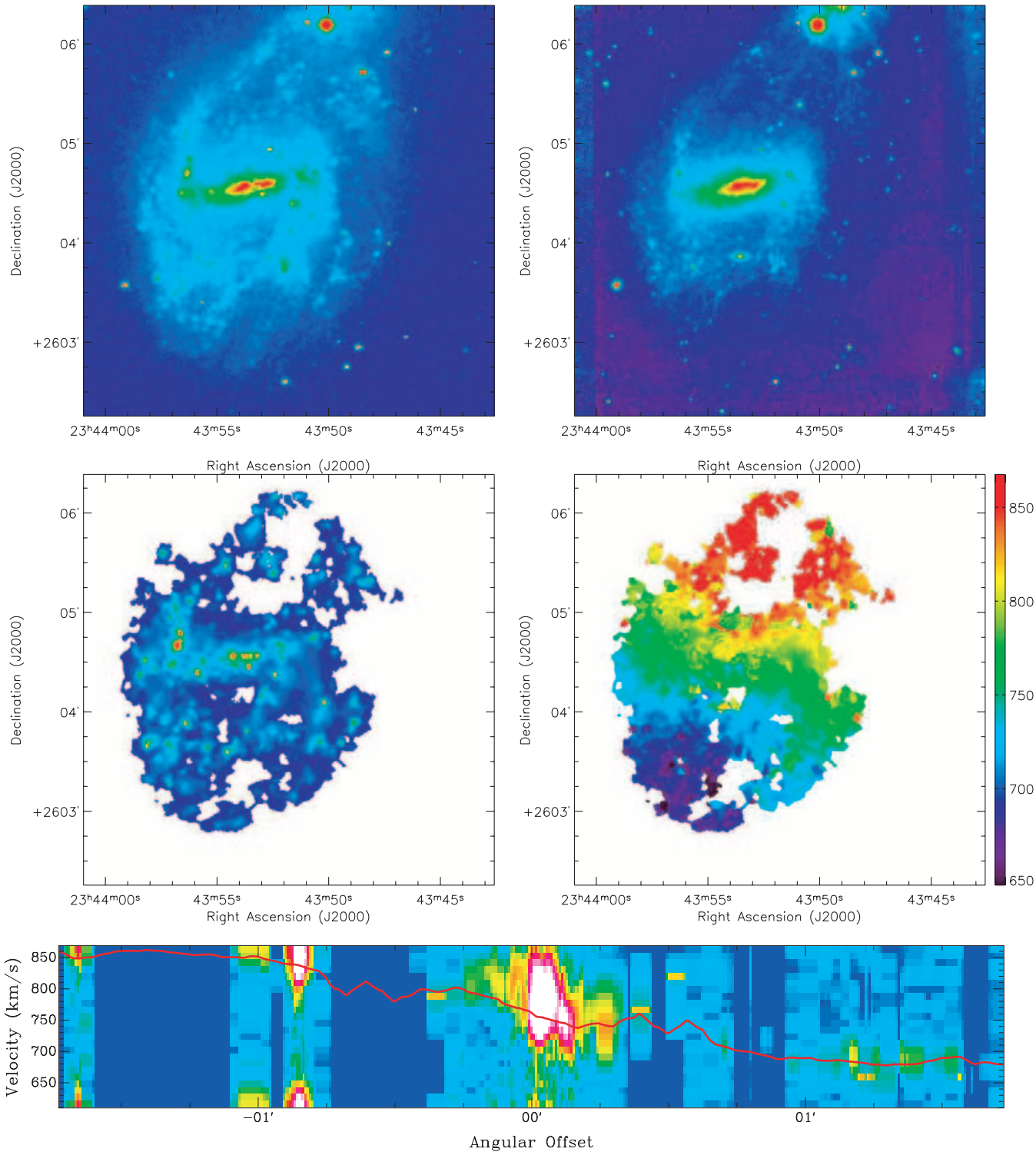

Figure 25. NGC 7741. Top left: *B*-band image from Knapen et al. (2004). Top right: K_s-band image from Knapen et al. (2003). Middle left: Hα monochromatic image. Middle right: Hα velocity field. Bottom: PV diagram.

our study will differ in two major aspects. First, their comparison is relative to a small sample, whereas BHαBAR is homogeneous and well distributed over the Hubble sequence. Secondly, they only used long-slit data, whereas Hα velocity fields and Hα monochromatic images will be used to provide more accurate results, avoiding, for example, the uncertainties on PA and *i* present in one-dimensional data. This will be the first step toward the determination of accurate mass models for barred spiral galaxies, until the time when full 2D mass models using the whole velocity fields become available.

All the data presented in the paper will be available for the community once Papers II–IV are published.

Downloaded from https://academic.oup.com/mnras/article/360/4/1201/1076455 by CNRS - ISTO user on 26 January 2021

Table 4. Analysis of the residuals. $\overline{m}_{idwb}$ is the mean of the residual map in the disc part, using the model with the bar. $\overline{m}_{idab}$ is the mean of the residual map in the disc part, using the model avoiding the bar. $\overline{\sigma}_{idwb}$ is the dispersion of the residual map in the disc part, using the model with the bar. $\overline{\sigma}_{idab}$ is the dispersion of the residual map in the disc part, using the model avoiding the bar.

Galaxy	$\overline{m}_{idwb} - \overline{m}_{idab}$ (km s^{-1})	$\overline{\sigma}_{idwb}$ (km s^{-1})	$\overline{\sigma}_{idab}$ (km s^{-1})	Remarks
NCG 0925	+5.2	30.6	17.0	
IC 0342	n/a	n/a	n/a	Bar not well defined
NGC 1530	+11.4	51.6	31.6	
NGC 2336	n/a	n/a	n/a	No Hα in the bar region
NGC 2403	n/a	n/a	n/a	Bar not well defined
NCG 2903	+1.0	20.3	19.8	
NGC 3198	+0.20	12.0	10.6	
NCG 3359	+1.0	21.5	12.9	
NGC 3953	+2.2	27.3	14.0	
NGC 3992	n/a	n/a	n/a	No Hα in the bar region
NGC 4236	5.8	21.4	10.8	
NGC 4321	+0.8	15.6	13.8	
NGC 4535	+0.7	16.5	13.4	
NGC 5371	n/a	n/a	n/a	No Hα in the bar region
NGC 5457	1.1	33.7	33.0	
NGC 5921	n/a	n/a	n/a	No Hα in the bar region
NGC 5964	+2.8	25.9	16.7	
NGC 6217	+2.6	20.7	13.8	
NGC 6946	+1.1	18.5	13.3	
NGC 7479	+30.2	108.7	103.56	'Broken arm' in the disc region
NGC 7741	+4.9	19.5	14.5	

Table 5. H I, kinematical and photometrical position angles and inclinations. Offsets between kinematical and photometrical centres. PA is the position angle of the major axis of the galaxy. † indicates that PA = 180°; – kinematical PA. ∗ indicates that PA = 180° + kinematical PA. References for H I data are as follows: (1) Pisano, Wilcots & Elmegreen (1998); (2) Crosthwaite, Turner & Ho (2000); (3) Teuben et al. (1993); (4) WHISP data (van der Hulst, van Albada & Sancisi 2001); (5) Schaap, Sancisi & Swaters (2000); (8) Ball (1986); (9) Verheijen & Sancisi (2001); (10) Bottema & Verheijen (2002); (11) Shostak (1973); (12) Knapen et al. (1993); (13) Guhathakurta et al. (1988); (14) Zasov & Silchenko (1987); (15) Bosma, Goss & Allen (1981); (16) Schulman, Bregman & Roberts (1994); (17) Hewitt, Haynes & Giovanelli (1983); (18) van Driel & Buta (1991); (19) Carignan et al. (1990); (20) Laine & Gottesman (1998).

Galaxy	H I		Ref.	Photometrical		Hα kinematical		Offset from photo. centre	
name	PA (°)	Incl.(°)		PA (°)	Incl.(°)	PA (°)	Incl.(°)	(arcsec)	(kpc)
NGC 0925	101.0±1.0*	58.5	1	102	57.6	105.0±1.0*	57.8±1.5	26.0	0.670
IC 0342	37±1.0	31±6.0	2	n/a	12.0	42.0±2.0	29.0±0.4	16.2	0.830
NGC 1530	n/a	58	3	n/a	60.3	5.0±1.0*	47.6±0.6	2.9	0.020
NGC 2336	n/a	59	4	178	58.5	177.0±1.3†	58.7±2.7	4.1	0.002
NGC 2403	124	61	5	127	57.5	125.0±1.0	60.0±2.0	25.4	1.167
NGC 2903	20*	61	4	17	63.6	22.0±1.0*	61.5±0.5	2.4	0.083
NGC 3198	36*	71	7	35	70.1	33.9±0.3*	69.8±0.8	8.4	0.105
NGC 3359	172†	51	8	170	54.5	167.0±2.0†	55.0±2.0	6.1	0.015
NGC 3953	11	58	9	13	62.2	13.0±0.8	59.0±0.4	6.5	0.086
NGC 3992	70±5*	57±1	10	68	53.5	67.0±1.0*	57.8±0.8	2.9	0.015
NGC 4236	163	75	11	162	74.4	156.1±1.6	76.1±0.7	55.5	0.498
NGC 4321	27±1†	27	12	30	16.5	27.0±1.0†	31.7±0.7	8.7	0.101
NGC 4535	3*	40	13	0	46.1	2.3±0.4*	35.0±2.0	3.6	0.057
NGC 5371	8	43	14	8	38.3	12.0±1.0	46.0±1.5	2.0	0.011
NGC 5457	49	18	15	n/a	15.3	53.0±1.0	20.0±2.0	17.7	0.297
NGC 5921	n/a	24	16	130	36.5	114.0±0.7	42.0±2.0	4.5	0.045
NGC 5964	144	41	17	145	40.0	138.7±0.7	38.8±2.1	15.0	1.130
NGC 6217	249	29	18	n/a	34.5	250.0±1.0	34.1±2.1	3.34	0.014
NGC 6946	240±1	38±5	19	n/a	32.4	239.0±1.0	38.4±3.0	8.2	0.163
NGC 7479	22	51	20	25	41.7	23.0±1.0*	48.2±1.3	7.2	0.060
NGC 7741	47	5	4	170	48.8	162.9±0.5*	46.5±1.5	3.9	0.023

Downloaded from https://academic.oup.com/mnras/article/360/4/1201/1076455 by CNRS - ISTO user on 26 January 2021

ACKNOWLEDGMENTS

We thank Chantal Balkowski for her help and support at the different stages of this work. We also thank Olivia Garrido, Jacques Boulesteix, Jean-Luc Gach, Philippe Balard and Olivier Boissin for their support. It is a pleasure to thank the OmM staff, in particular Bernard Malenfant and Ghislain Turcotte for their enthusiastic and competent support. Let us, also, acknowledge Pierre Martin and the CFHT team for their support at the top of the Mauna Kea. The FaNTOmM project has been carried out by the Laboratoire d'Astrophysique Expérimentale (LAE) of the Université de Montréal using a grant from the Canadian Foundation for Innovation and the Ministère de l'Education du Québec. This project made use of the LEDA data base (http://leda.univ-lyon1.fr/). The Digitized Sky Surveys were produced at the Space Telescope Science Institute under US Government grant NAG W-2166. The images of these surveys are based on photographic data obtained using the Oschin Schmidt Telescope on Palomar Mountain and the UK Schmidt Telescope.

REFERENCES

Amram P., Le Coarer E., Marcelin M., Balkowski C., Sullivan W. T., Cayatte V., 1992, A&APS, 94, 175
Artamonov B. P., Badan Y. Y., Bruyevich V. V., Gusev A. S., 1999, Astron. Rep., 43, 377
Arsenault R., Roy J.-R., Boulesteix J., 1990, A&A, 234, 23
Athanassoula E., 1984, Phys. Rep., 114, 321
Athanassoula E., Misiriotis A., 2002, MNRAS, 330, 35
Ball R., 1986, ApJ, 307, 453
Begeman K. G., 1987, PhD thesis, Rijuniversiteit, Groningen
Begeman K. G., 1989, A&A, 223, 47
Blais-Ouellette S., Carignan C., Amram P., Côté S., 1999, AJ, 118, 2123
Blais-Ouellette S., Amram P., Carignan C., 2001, AJ, 121, 1952
Blais-Ouellette S., Amram P., Carignan C., Swaters R., 2004, A&A, 420, 147
Bosma A., 1981a, AJ, 86, 1791
Bosma A., 1981b, AJ, 86, 1825
Bosma A., Goss W. M., Allen R. J., 1981, A&A, 93, 106
Bottema R., Verheijen M. A. W., 2002, A&A, 388, 793
Bottinelli L., Gouguenheim L., Paturel G., de Vaucouleurs G., 1983, A&A, 118, 4
Buta R., Crocker D. A., 1993, AJ, 105, 1344
Canzian B. J., 1990, PhD thesis, California Institute of Technology, Pasadena
Canzian B., Allen R. J., 1997, ApJ, 479, 723
Cappellari M., Copin Y., 2002, in Rosado M., Binette L., Arias L., eds, ASP Conf. Ser. Vol. 282, Galaxies: the Third Dimension. Astron. Soc. Pac., San Francisco, p. 515
Carignan C., Charbonneau P., Boulanger F., Viallefond F., 1990, A&A, 234, 43
Cayatte V., van Gorkom J. H., Balkowski C., Kotanyi C., 1990, AJ, 100, 604
Cepa J., Beckman J. E., 1990, A&AS, 83, 211
Combes F., Gerin M., 1985, A&A, 150, 327
Corradi R. L. M., Boulesteix J., Bosma A., Amram P., Capaccioli M., 1991, A&A, 244, 27
Crosthwaite L. P., Turner J. L., Ho P. T. P., 2000, AJ, 119, 1720
Curtis H. D., 1918, Publ. Lick. Obs., 13, 45
Daigle O., Carignan C., Hernandez O., Chemin L., Amram P., 2005, MNRAS, submitted
de Vaucouleurs G., 1963, ApJS, 8, 31
de Vaucouleurs G., de Vaucouleurs A., Corwin H. G., Buta R. J., Paturel G., Fouque P., 1991, Third Reference Catalogue of Bright Galaxies, Vols. 1–3, XII. Springer-Verlag, Berlin (RC3)
Elmegreen B. G., Wilcots E., Pisano D. J., 1998, ApJ, 494, L37
Eskridge P. B. et al., 2000, AJ, 119, 536
Ferrarese L. et al., 1996, ApJ, 464, 568
Fraternali F., Oosterloo T., Sancisi R., van Moorsel G., 2001, ApJ, 562, L47
Freedman W. L., Madore B. F., 1988, ApJ, 332, L63
Gach J.-L. et al., 2002, PASP, 114, 1043
Garcia-Burillo S., Sempere M. J., Combes F., Neri R., 1998, A&A, 333, 864
Garrido O., Marcelin M., Amram P., Boissin O., 2003, A&A, 399, 51
Gooch R., 1996, in Jacoby G. H., Barnes J., eds, ASP Conf. Ser. Vol. 101, Astronomical Data Analysis Software and Systems V. Astron. Soc. Pac., San Francisco, p. 80
Gottesman S. T., 1982, AJ, 87, 751
Guhathakurta P., van Gorkom J. H., Kotanyi C. G., Balkowski C., 1988, AJ, 96, 851
Hackwell J. A., Schweizer F., 1983, ApJ, 265, 643
Helfer T. T., Thornley M. D., Regan M. W., Wong T., Sheth K., Vogel S. N., Blitz L., Bock D. C.-J., 2003, ApJS, 145, 259
Hernandez O., Gach J., Carignan C., Boulesteix J., 2003, Proc. SPIE, 4841, 1472
Hernandez O., Wozniak H., Carignan C., Amram P., Chemin L., Daigle O., 2005, ApJ, submitted
Hewitt J. N., Haynes M. P., Giovanelli R., 1983, AJ, 88, 272
Hubble E. P., 1926, ApJ, 64, 321
Joye W., Mandel E., 1999, in Mehringer D. M., Plante R. L., Roberts D. A., eds, ASP Conf. Ser. Vol. 172, Astronomical Data Analysis Software and Systems VIII. Astron. Soc. Pac., San Francisco, p. 429
Kelson D. D. et al., 1996, ApJ, 463, 26
Kelson D. D. et al., 1999, ApJ, 514, 614
Knapen J. H., Cepa J., Beckman J. E., Soledad del Rio M., Pedlar A., 1993, ApJ, 416, 563
Knapen J. H., Beckman J. E., Heller C. H., Shlosman I., de Jong R. S., 1995, ApJ, 454, 623
Knapen J. H., Shlosman I., Heller C. H., Rand R. J., Beckman J. E., Rozas M., 2000a, ApJ, 528, 219
Knapen J. H., Shlosman I., Peletier R. F., 2000b, ApJ, 529, 93
Knapen J. H., de Jong R. S., Stedman S., Bramich D. M., 2003, MNRAS, 344, 527
Knapen J. H., Stedman S., Bramich D. M., Folkes S. L., Bradley T. R., 2004, A&A, 426, 1135
Kormendy J., 1983, ApJ, 275, 529
Laine S., Gottesman S. T., 1998, MNRAS, 297, 1041
Lütticke R., Dettmar R.-J., Pohlen M., 2000, A&A, 362, 435
Macri L. M. et al., 1999, ApJ, 521, 155
Marcelin M., Boulesteix J., Courtes G., 1982, A&A, 108, 134
Marcelin M., Boulesteix J., Georgelin Y., 1983, A&A, 128, 140
Martin P., 1995, AJ, 109, 2428
Martin P., Roy J., 1995, ApJ, 445, 161
Pérez I., Fux R., Freeman K., 2004, A&A, 424, 799
Peterson C. J., Thonnard N., Rubin V. C., Ford W. K., 1978, ApJ, 219, 31
Pisano D. J., Wilcots E. M., Elmegreen B. G., 1998, AJ, 115, 975
Rand R. J., 1995, AJ, 109, 2444
Rozas M., Zurita A., Beckman J. E., 2000a, A&A, 354, 823
Rozas M., Zurita A., Beckman J. E., Pérez D., 2000b, A&AS, 142, 259
Sakamoto K., Okumura S., Minezaki T., Kobayashi Y., Wada K., 1995, AJ, 110, 2075
Schaap W. E., Sancisi R., Swaters R. A., 2000, A&A, 356, L49
Schoenmakers R. H. M., Franx M., de Zeeuw P. T., 1997, MNRAS, 292, 349
Schulman E., Bregman J. N., Roberts M. S., 1994, ApJ, 423, 180
Sérsic J. L., 1973, PASP, 85, 103
Shostak G. S., 1973, A&A, 24, 411
Silbermann N. A. et al., 1994, Bull. Am. Astron. Soc., 26, 1353
Sofue Y., Tomita A., Tutui Y., Honma M., Takeda Y., 1998, PASJ, 50, 427
Teuben P., Regan M., Vogel S., van der Hulst T., Wainscoat R., 1993, Bull. Am. Astron. Soc., 25, 1411
Tremaine S., Weinberg M. D., 1984, ApJ, 282, L5
Tully R. B., 1988, J. Brit. Astron. Assoc., 98, 316
van der Hulst J. M., van Albada T. S., Sancisi R., 2001, in Hibbard J. E., Rupen M., van Gorkom J. H., eds, ASP Conf. Ser. Vol. 240, Gas and Galaxy Evolution. Astron. Soc. Pac., San Francisco, p. 451
van Driel W., Buta R. J., 1991, A&A, 245, 7

Downloaded from https://academic.oup.com/mnras/article/360/4/1201/1076455 by CNRS - ISTO user on 26 January 2021

van Moorsel G. A., 1983, A&AS, 54, 19
Verheijen M. A. W., Sancisi R., 2001, A&A, 370, 765
Vogt N. P., Haynes M. P., Herter T., Giovanelli R., 2004, AJ, 127, 3273
Wilke K., Möollenhoff C., Matthias M., 1999, A&A, 344, 787
Wynn-Williams C. G., Becklin E. E., 1985, ApJ, 290, 108
Zasov A. V., Silchenko O. K., 1987, SvA Lett., 13, 186
Zurita A., Relaño M., Beckman J. E., Knapen J. H., 2004, A&A, 413, 73

APPENDIX A: DESCRIPTION OF THE INDIVIDUAL GALAXIES

In this appendix we give a brief description of the structures observed in the Hα velocity fields and monochromatic images of the BHαBAR sample.

IC 0342. This large SAB(rs)cd nearby galaxy is nearly face-on so its photometrical PA is uncertain. A strong difference between its kinematical and photometrical inclination is noted. Observations in CO and H I (Crosthwaite et al. 2000) suggest that its kinematical PA is 37°. The kinematical data from CO, H I and Hα are comparable. An Hα spiral structure near the centre can be seen.

NGC 0925. This late-type SBcd galaxy has a bright optical and Hα bar and two bright patchy spiral arms beginning at the ends of the bar. Many H II regions lie along the bar. Photometrical and kinematical data agree. The PV diagram shows non-axisymmetric motions near the centre. It is well studied in H I (Elmegreen, Wilcots & Pisano 1998; Pisano et al. 1998), in CO (Helfer et al. 2003) and in Hα (Marcelin, Boulesteix & Courtes 1982). It shows strong streaming motions.

NGC 1530. This strongly barred spiral galaxy has been extensively studied by Zurita et al. (2004). Here, the FaNTOmM observation provides many more details of the kinematics along the major axis due to its large FOV and high sensitivity. A nuclear spiral and a large velocity gradient are observed. In the *V*-band images, a nuclear bar (Buta & Crocker 1993) with hotspots (Sérsic 1973) can be seen.

NGC 2336. NGC 2336 is an intermediate-type ringed barred spiral galaxy with a prominent bar. This galaxy shows a very regular morphological structure with no major asymmetries, except for the central regions where H I maps show a lack of gas in the centre (van Moorsel 1983). The Hα monochromatic image suggests the same lack. The NW part of the disc has been cut off by the wings of the interference filter. Although NGC 2336 belongs to an apparent pair of galaxies (together with IC 467) with a projected linear distance of 135 kpc, its undisturbed disc does not exhibit any distinct sign of recent interactions (Wilke, Möllenhoff & Matthias 1999).

NGC 2403. This SABc galaxy shows amorphous spiral features. The Hα velocity maps and the PV diagram show an almost rigid structure near the centre of the galaxy. Bright H II regions can be seen in the Hα monochromatic image. It is not clear whether this galaxy in barred or not. According to Schoenmakers et al. (1997), their Fourier harmonic analysis of the H I velocity field shows that non-circular motions are not important in this galaxy. Moreover, Schaap et al. (2000) stress that the thin hydrogen disc of NGC 2403 is surrounded by a vertically extended layer of H I that rotates slower than the disc. A complete modelling of the galaxy will provide more details on its structures. Fraternali et al. (2001) suggest that this anomalous H I component may be similar to a class of HVCs observed in the Milky Way. In CO data, no molecular gas is detected (Helfer et al. 2003).

NGC 2903. This starburst galaxy shows several peaks of star formation in the circumnuclear region. These peculiar 'hotspots' have been identified and described in different ways by various authors in Hα (Marcelin, Boulesteix & Georgelin 1983), in radio and in the IR by Wynn-Williams & Becklin (1985). A strong velocity gradient can be seen along the bar in the velocity map. The PV diagram shows a clear step in the RC. This step-like structure could be related to its strong bar. The molecular gas, visible in CO observations (Helfer et al. 2003), follows the bar.

NGC 3198. This SB(rs)c galaxy has been extensively studied in H I (Bosma 1981a; Begeman 1989), FP Hα (Corradi et al. 1991; Blais-Ouellette et al. 1999) and Hα and [N II] long-slit spectroscopy (Sofue et al. 1998; Vogt et al. 2004). According to the PV diagram, non-circular motions near the centre can be seen. A strong velocity gradient is also seen perpendicular to the bar major axis.

NGC 3359. NGC 3359 is a strongly barred galaxy. Its H II regions have been studied (Martin & Roy 1995) and catalogued (Rozas, Zurita & Beckman 2000a). The structure and kinematics of the H I were analysed in detail by Gottesman (1982) and Ball (1986) showing a clumpy distribution and a low surface density within the annular zone of strong star formation, which can be explained as due to the effect of the bar sweeping up gas as it rotates. Analysis of the Hα velocity map shows a disc with an axisymmetric rotation and also evidence of strong non-circular motions as confirmed by Rozas et al. (2000b). Analysis of the Hα residual velocity map (not shown here) shows strong streaming motions in the spiral arms and a strong gradient of gas in the bar.

NGC 3953. One of the most massive spirals of the M81 group, it has been studied in H I by Verheijen & Sancisi (2001). It is rather poor in H I and the surface density drops near D_{25}. Moreover, in CO (Helfer et al. 2003), the gas seems to be located in a ring at the near end of the bar. In Hα, the same lack of gas in the centre can be seen, whereas the arms are well developed.

NGC 3992. This galaxy is the most massive spiral of the M81 group. Its H I distribution is regular. It has a prominent bar and very well-defined spiral arms. It has a faint radial H I extension outside its stellar disc. There is a pronounced central H I hole in the gas distribution at exactly the radial extent of the bar (Bottema & Verheijen 2002), also visible in the Hα emission line. Some Hα can be seen toward the centre of the galaxy. It is not clear whether this feature could exist in H I because of the poor spatial resolution of the H I data measurements. Observations in CO (Helfer et al. 2003) stress the lack of molecular gas in the galaxy.

NGC 4236. This late-type SBdm galaxy is seen nearly edge-on. Its kinematical inclination is 76°. The Hα image shows that the H II regions are distributed along the bar, with two bright regions near the end of the bar. These features are also seen in H I (Shostak 1973). An extensive region of solid-body rotation coincides with the bar.

NGC 4321. This grand-design spiral galaxy has been frequently mapped in the *Hα* emission line using high-resolution FP interferometry (Arsenault, Roy & Boulesteix 1990; Cepa & Beckman 1990; Canzian & Allen 1997; Knapen et al. 2000a), in the molecular CO emission line (Canzian 1990; Rand 1995; Sakamoto et al. 1995; Garcia-Burillo et al. 1998; Helfer et al. 2003) and in the 21-cm H I emission line (Cayatte et al. 1990; Knapen et al. 1993). The H I disc is almost totally confined within the optical one but with a slight lopsidedness towards the south-west (Knapen et al. 1993). The H I, CO and Hα velocity fields show kinematical disturbances such as streaming motions along the spiral arms and a central S-shape distortion of the isovelocity contours along the bar axis. The circumnuclear region (CNR) and shows the presence of an enhanced star formation region as a four-armed Hα ring-like structure and a CO and Hα spiral-like structure. Many more details can be found in Hernandez et al. (2005).

Downloaded from https://academic.oup.com/mnras/article/360/4/1201/1076455 by CNRS - ISTO user on 26 January 2021

NGC 4535. With NGC 4321, this is another Virgo cluster galaxy with a known Cepheids distance (16.0 Mpc). It is not located in the main substructure of the cluster close to the core elliptical galaxy M87 but it lies in the southern extension related to M49. Although the Hα morphology appears perturbed, with an obvious indication of multiple spiral arms (these features are even present in the NIR K_s image), its velocity field is regular. No H I was found in the central parts (Cayatte et al. 1990).

NGC 5371. In this galaxy, there is no evidence of Hα emission in the centre.

NGC 5457. M101 is a large nearby galaxy. Observations of CO data (BIMA song; Helfer et al. 2003) show that the molecular gas is only distributed along the bar. In the Hα image the gas is distributed over the whole field. Two large arms can be seen.

NGC 5921. This galaxy shows a ring-like structure in both the Hα and the XDSS blue images. The bar is not clearly seen in Hα but many H II regions lie at the end of the bar. The centre of the galaxy is the host of a strong velocity gradient well defined in the Hα velocity map. Nevertheless, no Hα gas is present between the ring-like structure and the centre.

NGC 5964. This galaxy shows strong H II regions distributed along its bar. Nevertheless, no strong velocity gradient can be seen in this direction.

NGC 6217. This galaxy presents a prominent bar, with an important region of stellar formation on it located at 10 arcsec in the south-eastern direction from the galactic centre (Artamonov et al. 1999). The galactic centre reveals the presence of a different structural component, a ring. The size of the ring in Hα observations is approximately of 43 arcsec, which agrees with previous works in H I on this galaxy (van Driel & Buta 1991). The inner ring structure in the centre of the galaxy can be easily seen in the Hα monochromatic image.

NGC 6946. According to H I studies (Carignan et al. 1990), the H I distribution is not symmetric but is more extended to the north-east side. This feature is also seen in the Hα emission map. The overall Hα velocity map is regular but shows some non-circular motions near the centre, confirmed by the PV diagram. It has been recently observed in FP by Blais-Ouellette et al. (2004) leading to the same conclusions. Once again, the wide field of FaNTOmM and its high sensitivity is clearly an advantage to obtain better Hα velocity fields.

NGC 7479. This SB(s)c galaxy has been studied in H I by Laine & Gottesman (1998). The H I distribution shows considerable asymmetries and distortions in the outer disc. The H I and Hα kinematics suggest that, while the global velocity field is fairly regular, a severe perturbation is present in the western spiral arm. There is also a strong velocity gradient along the bar confirmed in the PV diagram. The Hα monochromatic image shows strong H II regions at one end of the bar.

NGC 7741. This galaxy shows a strong bar in the Hα, blue- and K_s-band images. Many H II regions are located along the bar. The velocity map clearly shows non-circular motions, whereas the velocity gradient is not too strong (compared with NGC 2903, for example).

This paper has been typeset from a TEX/LATEX file prepared by the author.

Downloaded from https://academic.oup.com/mnras/article/360/4/1201/1076455 by CNRS - ISTO user on 26 January 2021